Use of Lime-iron Sludge for Soil Modification

Beverly S. Chittoo[1], Clint Sutherland[2]

Project Management and Civil Infrastructure Systems Department, University of Trinidad and Tobago
San Fernando, Trinidad

[1]beverly.chittoo@utt.edu.tt; [2] clint.sutherland@utt.edu.tt

Abstract

The worldwide increase in production of water treatment sludge together with the overwhelming disposal cost has fuelled research into the development of economic re-use alternatives. This study investigated the shear behaviour of unmodified and modified clay to determine the potential of using lime-iron sludge as a soil modifier. The effects of lime-iron sludge concentration, moisture content and vertical normal stresses were examined.

The optimum dose of lime-iron sludge was found to be 3% with an accompanying optimum moisture content of 20%. An improvement of 20% increase in shear stress together with a rise in cohesion of 155% was observed. However, the inclusion of lime-iron sludge in soil specimens had no significant effect on the internal friction angle.

Experimental results were successfully used to illustrate the positive effect of lime-iron sludge inclusion on the shear behaviour of soil. Additionally, experimental data was successful in correlating shear variables and optimizing soil parameters to aid in the eventual development of full-scale design.

Keywords

Modified; Lime-iron Sludge; Direct Shear Test; Shear Stress; Peak Stress; Residual Stress; Inorganic Clay

Introduction

Increasing quantities of Water Treatment Sludge (WTS) are being produced worldwide due to increased water demand, more stringent controls over the quality of produced water and lack of suitable reuse for residuals.

WTS often defines the residual produced from water softening, chemical coagulation, flocculation, and settling processes used in the treatment of potable water (Twort *et al.* 2000). Added coagulants cause the impurities to aggregate into flocs that can be separated from the water, removing not only the impurities but also the chemical additives.

A popular approach to WTS disposal is to discharge into an excavated lagoon where it is left indefinitely. This is not a long-term solution as lagoons have a finite capacity and landfills occupy significant land space. Further, such solutions are a major financial burden to the water treatment plant due to cost of drying, loading, and transporting the sludge.

According to Moldan (1990) most environmental protection regulations require that the quantity of waste produced is minimized. If possible, the wastes should be re-used or processed as secondary raw materials as much as possible. Otherwise, the solid wastes should be put back in the environment where the space occupied should be as little as possible and minimum costs should be achieved.

Reported methods of soil modification include physical processes such as soil densification, blends with other material, use of reinforcements (Geogrids), and chemical processes such as mixing with cement, bituminous emulsions, fly ash, lime, lime by-products and blends of any one of these materials. (Soil Stabilization in Pavement Structures, 1979). Improved soil properties such as strength, plasticity, compressibility, deformation, hydraulic conductivity, workability, durability, swelling potential, and volume change tendencies have been reported.

Water treatment sludge may be classified as either lime sludge or lime-iron sludge. According to Benešová (2004), the typical average iron content of iron sludge is 19.5% while the typical average iron content of lime sludge is 1.88%. While numerous studies have been reported in the literature on the reuse of lime-sludge as a soil modifier, little has been reported on lime-iron sludge. Yu, Zhang and Cartweight (2010) conducted a pilot investigation on the beneficial utilization of lime-sludge for subgrade stabilization. The results of the investigation indicated little improvement in unconfined soil strength.

However the modification demonstrated positive effects in reducing the plasticity of soil and increasing its durability and deformation.

Watt and Angelbeck (1977), in a study of the effects of adding lime-sludge to a road sub-base aggregate, found that addition of 0.5 to 1.0% sludge produced maximum improvement to the seven-day cure and freeze/thaw unconfined compressive strengths. The mix design was 86% aggregate, 11% fly ash, 3% lime, and 0 to 3% sludge solids.

According to Baker et al. (2005) the use of lime-sludge as a soil modifier holds promises from both performance and economic aspects. The large amount of sludge available and the fact that it is inexpensive (essentially free) is very attractive if it can be used for soil modification in transportation constructions.

In this investigation the effect of lime-iron sludge as a soil modifier is reported. The characteristics of lime-iron sludge are determined using the Atterburg's limits, and direct shear testing. Experimental data was analysed in an attempt to explicate the correlation of shear variables and determine the optimum parameters to aid in the eventual development of full-scale design.

Test Program

Materials Used for Testing

Experimental studies were carried out using lime-iron sludge obtained from a water treatment plant located in central Trinidad. The material, which is not currently re-used, was produced from water treatment processes used for the removal of iron from ground water. Lime-iron sludge specimens were subsequently classified as inorganic silt of low plasticity according to the Unified Soil Classification System. This lime-iron sludge was tested as a modifier using a soil obtained from the Northern Range of Trinidad. The soil was classified as inorganic clay of medium plasticity according to the Unified Soil Classification System.

Methodology

This study examined the shear behaviour of unmodified and modified soil specimens. The main variables considered in the tests are as follows:

- Lime-iron sludge concentration
- Moisture content
- Vertical normal stress

Samples of soil and/or lime-iron sludge were classified using the multipoint liquid limit method of the Standard Test Methods (ASTM D4318).

The Standard Test Method for Direct Shear Test of Soils under Consolidated Shear Condition, (ASTM D3080) was performed using a direct shear machine (ELE International T206) to characterize the shear parameters presented in this paper. The tests were conducted in a shear box 5.0 cm by 5.0 cm in plane and 4.2 cm in depth. The shearing rate was 0.001 cm/s. Shear stresses were recorded up to a horizontal displacement of 1.2 cm in order to observe the post-failure behaviour.

Prior to definition of the effects of the shear parameters, all specimens were compacted with the same compactive effort according to ASTM D698 standard using a 10.0 cm diameter by 15.0cm wide mould. The moisture content was determined by oven (ELE 13578) drying.

Sample Preparation

Prior to laboratory testing the lime-iron sludge and soil were dried at 105⁰C and then pulverized in a mortar and pestle. The specimens were left in the laboratory for 24 hours to attain equilibrium moisture content, which was found to approximate 12%. The moisture content was verified periodically.

Results and Discussion

The Effect of Lime-iron Sludge on the Index Properties of Inorganic Clay

The index properties of the soil and lime-iron sludge determined according to ASTM D4318 are summarized in Tables 1 and 2 respectively.

TABLE 1 INDEX PROPERTIES OF SOIL

Characteristics	
Soil Type	Inorganic clay of medium plasticity
Liquid Limit	41.40
Plastic Limit	28.24
Plasticity Index	13.16

TABLE 2 INDEX PROPERTIES OF LIME-IRON SLUDGE

Characteristics	
Soil Type	Inorganic silt of low plasticity
Liquid Limit	66.00
Plastic Limit	53.00
Plasticity Index	13.00

Modified specimens were prepared using soil and 3% lime-iron sludge. The index properties of modified specimens determined according to ASTM4318 are

summarized in Table 3. Experimental data indicated that inclusion of lime-iron sludge had a significant effect on liquid limit and plasticity. An increase of 17% in liquid limit together with an increase in plasticity of 43% was obtained. This change in properties may increase the degree to which the material can be moulded or reworked to cause permanent deformation before rupture. A marginal 4% increase in plastic limit was obtained indicating that inclusion of lime-iron sludge has little effect on the dryness of the material.

TABLE 3 INDEX PROPERTIES OF MODIFIED SPECIMENS

Characteristics	
Soil Type	Inorganic clay of medium plasticity
Liquid Limit	48.25
Plastic Limit	29.37
Plasticity Index	18.88

The Effect of Moisture Content on the Shear Stress of Modified soil

The optimum moisture content, that is, the moisture content that leads to the maximum soil density under the particular test conditions was determined by varying the moisture content as well as the percentage addition of lime-iron sludge. The percentage lime-iron sludge was varied between 0% and 10% at a normal stress of 6.38 kN/m². Figure 1 shows the shear stress values obtained when the moisture content was varied between 10% and 30% of the dry weight of modified and unmodified specimens. The results indicated that the increment in the concentration of lime-iron sludge in the soil matrix increased both the shear stress and optimum moisture content.

For unmodified specimens the optimum moisture content was found to be 18%. Modified specimens prepared with 3% lime-iron sludge produced an optimum moisture content of 20%. From Figure 1 it is also observed that a 5% change in moisture content above or below the optimum value results in a significant change in shear stress. At low moisture content a reduced value of shear stress was recorded which may have been due to a decrease in density and thus the need for an increased compactive effort. On the other hand, excessive volumes of water within the soil matrix may have resulted in reduced interlocking and bonding of particles. Hence the soil expanded its volume and the density of the soil particles as well as the shear stress decreased.

By connecting the peak on each curve, a line of optimum moisture content is drawn which enables the determination of optimum moisture content for any lime-iron sludge concentration between 0 and 10%.
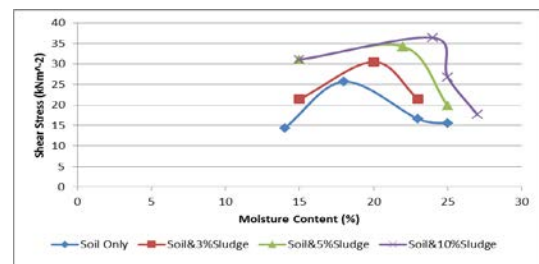

FIG. 1 EFFECT OF MOISTURE CONTENT ON THE SHEAR STRESS OF INORGANIC CLAY FOR DIFFERENT LIME-IRON SLUDGE CONCENTRATIONS

The Effect of Lime-iron Sludge Addition on the Stress-strain Curves of Modified Soil

Figure 2 shows the stress-strain curves obtained when the added amount of lime-iron sludge was varied between 0% and 15% at a normal stress of 6.38 kN/m².

The effect of lime-iron sludge addition at constant compaction showed that the shape of the stress-strain curves differed significantly to that of unmodified specimens. Unmodified soil showed a well defined curve with increasing shear resistance with shear displacement until a constant value was reached. No peak shear stress was obtained over the range of displacement tested. A peak stress was obtained for each sample containing lime-iron sludge, which reduced with continued shearing until the residual stress was reached. A ductile shear interface in which the specimens continue to deform after reaching its peak stress was observed.

Rise in lime-iron sludge concentration between 0% and 10% resulted in an increase in stiffness (i.e., the rate of mobilization of strength with displacement), peak stress and residual stress. As shown in figure 2 the shear stress of the unmodified soil specimens was 25.675 kNm-3. Addition of 3% lime-iron sludge resulted in the formation of a peak stress, 20% beyond unmodified soil stress. The residual stress was 8% beyond that of the unmodified soil. A maximum of 40% increase in peak stress was obtained for modified specimens containing 10% lime-iron sludge.

At 15% lime-iron sludge addition the stress-strain curve initially fell below that of unmodified soil indicating a possible reduction in stiffness. However this modified sample subsequently displayed a gradual increase in residual stress over that of the other specimens tested. This increase may be the result of particle reorientation at the failure surface or changes in the volume of material within the shear
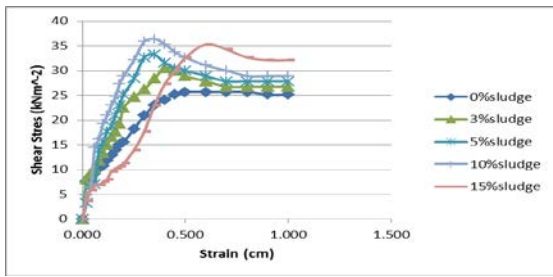
zone.

FIG. 2 EFFECT OF VARYING LIME-IRON SLUDGE CONCENTRATIONS ON THE STRESS-STRAIN CURVES AT OPTIMUM MOISTURE CONTENT

The Effect of Lime-iron Sludge on the Failure Envelopes Modified Soil

The Mohr-Coulomb failure envelopes for unmodified and modified specimens at varying normal stresses are presented in Figure 3. Modified specimens were prepared by varying the addition of lime-iron sludge between 0% and 10% and blending at the respective optimum moisture content. As shown in Figure 3, the shear stress increased linearly as the normal load was increased for both modified and unmodified specimens. Under increasing normal stress, soil particles tend to become denser and closer to lime-iron sludge particles thus resulting in greater shear resistance. The failure envelop appears to be linear for normal stresses of 5.10 kN/m², 6.38 kN/m² and 7.66 kN/m².

The results as presented in Figure 3 also indicated that inclusion of lime-iron sludge in soil specimens had minimal effect on its friction angle, which is indicated by the relatively parallel relationship of modified specimens. The friction angles were maintained at 59° for increasing concentrations of lime-iron sludge with the exception of specimens containing 2% lime-iron sludge. This specimen was deviated slightly producing a friction angle of 56°. The variation however may have been due to experimental error.

The inclusion of lime-iron sludge in soil specimens had a significant influence on the development of cohesion (Figure 4). The addition of 2% lime-iron sludge resulted in a 61% increase in both shear stress and cohesion. While the addition of 3% lime-iron sludge increased the cohesion and shear stress by 155%. Increasing the lime-iron sludge concentration beyond 3% resulted in only a marginal increment in cohesion. Thus, 3% lime-iron sludge was selected as the optimum dosage. This observed improvement in the cohesion intercept may have resulted from the developed anchorage forces and interlocking of soil particles.
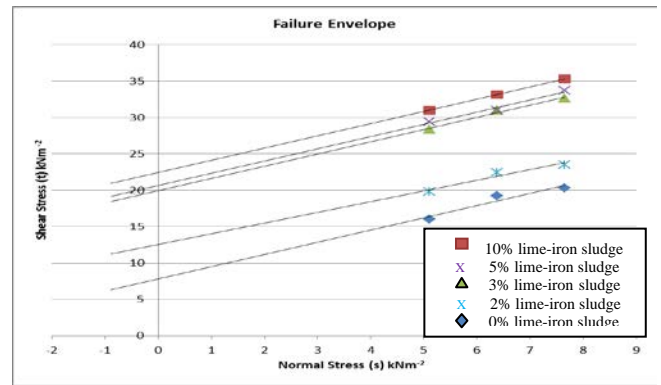

FIG. 3 FAILURE ENVELOPES OF UNMODIFIED AND MODIFIED SOIL AT OPTIMUM MOISTURE CONTENT
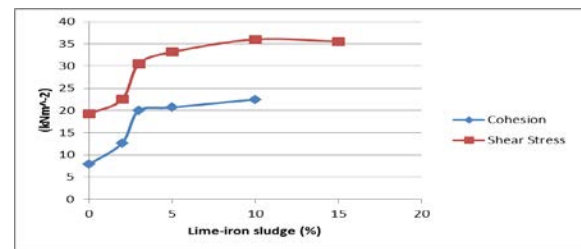

FIG. 4 EFFECT OF LIME-IRON SLUDGE ON THE SHEAR STRESS AND COHESION OF AN INORGANIC CLAY

The Effect of Normal Stress on the Shear Stress of Modified Soil

The effect of normal stress was investigated using specimens prepared at an optimum lime-iron sludge concentration of 3% and an optimum moisture content of 20%. The normal stresses were 5.10 kN/m², 6.38 kN/m² and 7.66 kN/m². The shear stress vs. horizontal displacement curves obtained for unmodified and modified specimens are presented in Figure 5.

A significant increase in initial steepness of curves was observed for all modified specimens when compared to unmodified specimens. This increase indicated that the inclusion of lime-iron sludge resulted in rise in the sample stiffness regardless of the normal stress applied. Mobilized strength increased gradually with increasing normal stress for both modified and unmodified specimens. This was illustrated by the leftward shift of the curves as the normal stress was increased.

There was no observed peak stress over the range of normal stress tested for unmodified specimens. A clear peak stress was obtained for each sample containing 3% lime-iron sludge, which reduced with continued shearing until the residual stress was reached. An increase in both peak stress and residual stress was obtained as the normal stress was increased. There was an approximate 10% increment in peak stress as the normal stress was increased from 5.10 kN/m² to 6.38 kN/m² and from 6.38 kN/m² to 7.66

kN/m^2, resulting in 20% increase in residual stress and an approximate 10% increase in residual stress, respectively. This change in peak stress and residual stress may have resulted due to an increase in the number of contact points between particles and a subsequent increase in particle resistance.
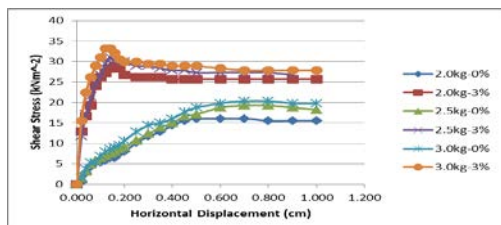

FIG. 5 STRESS VS. HORIZONTAL DISPLACEMENT CURVES FOR UNMODIFIED AND MODIFIED SOIL WITH 3% LIME-IRON SLUDGE AT VARYING NORMAL LOADS

Conclusions

This study was undertaken to investigate the shear behaviour of modified and unmodified clay to determine the potential of using lime-iron sludge as a soil modifier. The effects of lime-iron sludge concentration, moisture content and vertical normal stresses were examined. Based on the output of the research the following conclusions may be drawn:

- Compared to unmodified soil, modified specimens showed increment in shear stress with increasing concentration of lime-iron sludge within the range from 2 to 15%.

- The optimum lime-iron sludge concentration was found to be 3% with a corresponding optimum moisture content of 20%.

- The inclusion of 3% lime-iron sludge resulted in an 8% increase in residual stress over that of unmodified specimens. Further, modified specimens exhibited the development of a peak stress for all values of applied normal load. Addition of 3% lime-iron sludge resulted in the formation of a peak stress, approximately 20% beyond unmodified soil stress.

- The inclusion of lime-iron sludge as a soil modifier resulted in a significant improvement on the cohesion intercept. At optimum lime-iron sludge concentration 3% there was 155% increase in cohesion. However no noticeable change was observed with regard to the friction angles of modified specimens.

REFERENCES

Baker, Rob J., Van Leeuwen, J (Hans) and White, David J. Applications for Reuse of Lime Sludge from Water Softening. Final Report for TR-535. Iowa Department of Transportation Highway Division and the Iowa Highway Research Board, 2005.

Benešová, l., Runštuk, J., Tonika, J.: Nakládání s vodárenskými kaly a trendy využití v budoucích letech. Sborník konference Pitná voda (2004), Handling of Water Treatment Sludge and Trends in Future Use of the Sludge p. 117 – 131.

Moldan, B. Životní prostředí České republiky. 1.vydání. Praha: Academia, (1990), Environment of the Czech Republic 228 s. ISBN 80-200-0229-8

"Soil Stabilization in Pavement Structures", FHWA - 1P. 80-2, Vol. 2, Mixture Design Considerations, FHA, Office of Development Implementation Division, 1979.

Twort, A.C., Ratnayaka, D.D., and Brandt, M.J. (2000). Water supply. 5th ed. Arnold, London.

Watt, R. D., Angelbeck, D. I. (1977) "Incorporation of a Water Softening Sludge IntoPozzolanic Paving Material," Journal of American Water Works Association, March:175

Xiong (Bill) Yu, Bin Zhangand Donald Cartweight (2010) "Beneficial Utilization of Lime Sludge for Subgrade Stabilization: A Pilot Investigation", for the Ohio Department of Transportation Office of Research and Development.

Beverly Chittoo obtained her BASc. Degree in Civil Engineering Systems from the University of Trinidad and Tobago in 2011. She is currently pursuing a MPhil. at the University of Trinidad and Tobago specializing in Environmental Engineering in which she works as a Research Assistant in the department of Project Management and Civil Infrastructure Systems.

Clint Sutherland is an Assistant Professor at the Project Management and Civil Infrastructure Systems Unit of the University of Trinidad and Tobago. He is a former Trinidad and Tobago national scholar and graduated with honors with a BSc. in Civil Engineering in 1998 and a PhD in Civil and Environmental Engineering in 2004 from the University of the West Indies, St Augustine Trinidad. His PhD thesis was on the subject of "Removal of Heavy Metals using Low-Cost Adsorbents". He presently lectures in the area of Water

and Wastewater Engineering. His current research interest is in the areas of Remediation, Waste Reuse, Leaching, Water and Wastewater Engineering.

Effects of Cu Feedstock on Intermetallic Compound Formation in Cold Sprayed Cu-Sn Coatings

K. H. Ko[1], H. Lee[2], J. O. Choi*[3]

Department of Materials Science and Engineering, Ajou University, Suwon 443-749, Korea

[1]khko@ajou.ac.kr; [2]materialist@empal.com; *[3]cjo16@lycos.co.kr

Abstract

Cu-Sn composite coatings were deposited using various Cu feedstock powders with different sizes and shapes, and the formation of intermetallic compounds (IMCs) in the coatings was investigated. IMC formation by post-annealing of composite coatings could be affected. In addition, when Cu-Sn composite particles were employed, not only the Cu-Sn composites but also Cu-Sn IMCs (Cu_6Sn_5 and Cu_3Sn) were observed at the interfaces between Cu and Sn particles in the as-sprayed state. In the case of the annealed Cu-Sn coatings, the Cu_6Sn_5 formed in the as-coated coatings was transformed into the Cu_3Sn phase, and the embedded Sn particles were fully changed into the Cu_3Sn phase. However, the intermetallic compound formation of Cu_3Sn was different, depending on the shape and size of the Cu feedstock. Therefore, the deposition of Cu-Sn composite coatings using different Cu particles could have an influence on the formation of IMCs.

Keywords

Cold Spray; Cu-Sn; Composites; Intermetallic; Coatings

Introduction

In the thermal spray process, metallic and ceramic powders are melted by jets emitting hot gas with very high temperatures, after which coatings are formed through the solidification of the melted powders on the substrates. In the cold spray process, however, metallic powders are injected into a de Laval-type nozzle where they are accelerated to high velocities by a supersonic gas stream. When the metallic powders are impinged onto the substrate, their kinetic energy enables the production of coatings with severe deformation. Because the particles are deformed by collision with the substrate, ductile metallic powders must be chosen for the feedstock materials. Also, ceramic powders are unsuitable for feedstock materials in the cold spray process owing to the brittleness. However, in the case of metal (Al)/metal composites coated by the cold spray process, it is very easy to obtain high quality composite coatings because of the deformation behavior. In addition, intermetallic compounds (IMCs) in the coatings are easily obtained by post-annealing, as reported by many researchers. Wang et al. reported the characteristics and influence of heat treatment in Al/Fe composite coatings. Novoselova et al. reported the morphology, porosity, and hardness of Al/Ti composite coatings. Lee et al. investigated the formation of IMCs by post-annealing on cold sprayed Al/Ni and Al/Ti composites. In another case, intermetallic formation was realized by the interaction between the cold sprayed coatings and the substrates. H. Lee et al. reported the Al/Ni interface interaction for intermetallic compound formation produced by cold spraying and post-annealing. H. Bu et al. and K. Spencer et al. investigated the post treatments of Al coating/Mg substrate couples by cold spraying. In the case of Cu/metal composite coatings, few reports were available concerning Cu composite coatings by means of the cold spray process and their IMC formation by means of post-annealing. In this study, Cu-Sn composite coatings were deposited by cold spray on Al substrates, using various types of Cu powders, and annealing studies were carried out to transform the composite coatings into intermetallic compounds. Further, the properties of as-coated and annealed coatings were investigated. The results of these Cu-Sn coatings in the course of the cold spray will be applied in lead-free solders for flip chip connections and the anode electrodes for secondary batteries (Li ion batteries).

Experimental

A home-installed cold spray system was used in this work. The particles were accelerated through a converging–diverging de Laval-type nozzle with a throat diameter of 1 mm (inlet diameter, 7 mm). Pure air, instead of the usual helium and nitrogen, has been

used as both accelerating gas and powder feeding gas. The pressure before entering the gas heater was fixed at 2.0 MPa and the temperature of the gas passing through the nozzle ranged from 200 to 450ºCwhich was measured in the nozzle beside the feedstock feed entrance. The distance between the nozzle and the substrate was 20 mm. The substrate and nozzle were stationary during deposition, and therefore, the deposit was formed in a mountain-like shape. The particle sizes and shapes of as-purchased Sn and Cu were confirmed by scanning electron microscopy (SEM). The Cu-Sn composites were coated onto Al substrates without sand-blasting. The deposition efficiency of the Sn feedstock was higher than that of the Cu feedstock. To produce Cu matrix coatings, a Cu-Sn composite must contain an overwhelming composition of Cu. Therefore, the powder composition ratio of Cu and Sn was 90:10 wt%. The coated samples were annealed at 300ºC under N_2 atmosphere for 6 hours. The annealing heating rate was 5ºC/min and followed by furnace cooling. The structures of the Cu-Sn composite and annealed coatings were analyzed by X-ray powder diffractometry (XRD, Rigaku), and the microstructures and compositions of the coatings were measured by field emission-scanning electron microscopy (FESEM) with energy dispersive spectroscopy (EDS, Philips, XL 30 ESEM-FEG) and optical microscopy (OM).

Results and Discussion

Fig. 1 shows SEM images of the as-purchased Cu and Sn powders used in these experiments. The smaller Cu powders were under 10 μm with spherical shape, while the larger Cu powders were under 44 μm with dendritic shape (Figs. 1(a) and 1(b)). The micro-sized Sn powders were sieved to –325 mesh (≤44 μm) with irregular shape (Fig. 1(c)). Fig. 2 shows XRD patterns of cold sprayed Cu-Sn composite coatings using Cu powders with different shapes and sizes. Peaks corresponding to a newly formed phase were present, suggesting significant chemical interactions among Cu/Sn particles during coating, regardless of the Cu particles' properties. In particular, two types of Cu-Sn intermetallic compounds, Cu_6Sn_5 and Cu_3Sn, without the oxides (SnO, CuO), were observed. In addition, the Cu and Sn feedstock seemed to be neither molten nor semi-molten (Sn melting point: 232ºC) because their flight/coating time was extremely short, so the temperature of the coatings did not reach the melting point of Sn even though the gas temperature was

450ºC. Empirically, when the coatings were exposed to hot gas stream of 450ºC for 10 seconds, the Sn feedstock were melted on the substrate. If the Sn was melted, the coatings would be destroyed (similar to the morphology of thermal sprayed coatings). While coating was made post-annealing, the Cu_6Sn_5 phase disappeared and only Cu_3Sn peaks were observed after complete reaction of the embedded Sn. The Gibbs free energies of the Cu_3Sn and Cu_6Sn_5 phases were negative values, and the Gibb's free energy of the Cu_3Sn phase was lower than that of the Cu_6Sn_5 phase. Fig. 3 shows the OM images of the as-coated Cu-Sn composite coatings by cold spray under different conditions. Similar to the cases of other composite coatings by cold spray, such as Al-metal and Al-ceramic coatings, the "embedded particles phenomena" of Sn particles were observed, accompanied by severe plastic deformation and possible inter-particle bonding between Cu and Sn in the Cu matrix. In spite of the type of the Cu powder and the gas temperature conditions, significant differences in morphology were not observed. Only the plastically deformed and embedded Sn particles (without melting) were found in the Cu matrix despite an increased gas temperature of 450ºC. In addition, it is likely that the embedded soft Sn particles which had high strain energy could interact with the Cu matrix. However, the annealed Cu-Sn composite coatings seemed to differ with respect to Cu powder shape (Fig. 4). It was found that, in the as-coated state, the embedded Sn particles, including the intermetallic compounds (Cu_6Sn_5/Cu_3Sn) reacted with the Cu matrix and grown in the Cu-Sn coatings by using the smaller Cu powders (10 μm). Therefore, the annealed intermetallic compounds (Cu_3Sn) were coarser than the as-coated Sn/IMC particles (Sn/Cu_6Sn_5/Cu_3Sn). Despite the changes in the gas temperature, these results seemed to be the same in all of the annealed Cu-Sn coatings obtained using the smaller Cu powders. It was assumed that the diffusion path of the embedded Sn particles could be provided by the defects resulting from the strain of the smaller Cu (10 μm)-Sn coating systems. In contrast, in the larger Cu (44 μm)-Sn coating systems, the coarsening effect of the embedded Sn particles by post-annealing was less significant than that of the embedded Sn particles in the smaller Cu (10 μm)-Sn coatings. From these results, it was considered that the diffusion route of Sn particles into the Cu matrix or the interaction between Sn and the Cu matrix was very different according to the type of Cu powder.

In order to clearly confirm the compositions and phases of the as-coated and annealed Cu-Sn coatings, coatings prepared under different conditions were measured by the backscattered electron imaging and EDS. Fig. 5 and Fig. 6 show the EDS and backscattered images of the as-coated Cu-Sn coatings, in which the intermetallic compounds were found at the interfaces between Cu and Sn, regardless of gas temperature. Most interestingly, the IMCs of Cu_6Sn_5/Cu_3Sn (confirmed by XRD (Fig. 2)) were formed by the diffusion of Cu particles that were impacted into the Sn particles. Compared to the XRD data, it was also confirmed that the mixed IMCs of Cu-Sn (Cu_6Sn_5/Cu_3Sn) were detected by EDS at the interfaces, and residues of Sn were also observed. Fig. 7 and Fig. 8 show the EDS and backscattered images of the annealed Cu-Sn coatings. The results of the images and EDS were in agreement with the OM and XRD data. To prove that the smaller Cu powders (10 μm) were more severely deformed than the larger Cu powders (44 μm) by the high velocity impact, pure Cu coatings were deposited using both the finer and the coarser powders under the same deposition conditions as the Cu-Sn composite coatings (Fig. 9). As mentioned above, more severe deformation occurred with the smaller Cu particles than that with the larger Cu particles during spraying. As a result of these phenomena, the pores in the Cu coating prepared from the larger Cu powders were easily identified by the lower extent of deformation. Therefore, it was concluded that the more severe deformation as a result of the high velocity of the Cu particles could supply the energy for the coarsening of the IMC (the faster diffusion).

Conclusions

It has been shown that the as-coated and annealed Cu-Sn composites were prepared under different coating conditions (such as the gas temperature and type of Cu powder) on Al substrates by cold spray. In our study of the as-coated Cu-Sn composites, regardless of the type of Cu particles, both raw materials displayed desirable mechanical energy capacities during the high-velocity impact collision coating and could accumulate enough potential energy to overcome the activation barrier of in the course of compounding. Thus, from these results, intermetallic compounds of Cu-Sn in the as-coated state could be obtained at the interfaces between Cu and Sn by high velocity impact. In addition, a greater coarsening of the embedded Sn

particles by post-annealing was found for the smaller Cu (10 μm)-Sn composite coatings, which may be due to the higher energy of the smaller Cu particles having the capability to overcome the compounding activation barrier by high velocity impact.

REFERENCES

Bakshi, Srinivasa R., Laha, Tapas, Balani, Kantesh, Agarwal, Arvind, and Karthikeyan, Jeganathan. "Effect of Carrier Gas on Mechanical Properties and Fracture Behaviour of Cold Sprayed Aluminium Coatings." Surface Engineering 23 (2007): 18-22. Accessed January, 2007. doi: 10.1179/174329407X161618.

Bu, Hengyong, Yandouzi, Mohammed, and Jodoin, Bertrand. "Effect of Heat Treatment on the Intermetallic Layer of Cold Sprayed Aluminum Coatings on Magnesium Alloy." Surface and Coatings Technology 205 (2011): 4665-71. Accessed April 3, 2011. doi: 10.1016/j.surfcoat.2011.04.018.

Chidambaram, Vivek, Hald, John, and Hattel, Jesper Henri. "Development of Gold Based Solder Candidates for Flip Chip Assembly." Microelectronics Reliability 49 (2009): 323-30. Accessed December 21, 2008. doi: 10.1016/j.microrel.2008.12.012.

Chiu, TsungChieh, and Lin, KwangLung. "The Difference in the Types of Intermetallic Compound Formed between the Cathode and Anode of a Sn-Ag-Cu Solder Joint under Current Stressing." Intermetallics 17 (2009): 1105-14. Accessed May 26, 2009. doi: 10.1016/j.intermet.2009.05.014.

Cui, WangJun, Wang, Fei, Wang, Jie, Liu, Jaijing, Wang, Congxiao, and Xia, Yongyao. "A Modified Carbothermal Reduction Method for Preparation of High-Performance Nano-Scale Core-Shell Cu_6Sn_5 alloy Anodes in Li-ion Batteries." Journal of Power Sources 196 (2011): 3633-9. Accessed Desember 10, 2010. doi: 10.1016/j.jpowsour.2010.12.025.

Gärtner, Frank. "Advances in Cold Spraying." Surface Engineering 22 (2006): 161-3. Accessed June, 2006. doi: 10.1179/174329406X108906.

Guo, Zhongnan, Hindler, Michael, Yuan, Wenxia, and Mikula, Adolf. "Thermodynamic Properties of Liquid Au-Cu-Sn Alloys Determined from Electromotive Force Measurements." Thermochimica Acta 525 (2011): 183-9. Accessed August 8, 2011. doi: 10.1016/j.tca.2011.08.011.

Islam, M. N., Chan, YanCheong, Rizvi, M. J. and Jillek, Werner. "Investigations of Interfacial Reactions of Sn-Zn based and Sn-Ag-Cu lead-Free Solder Alloys as Replacement for Sn-Pb Solder." Journal of Alloys and Compounds 400 (2005): 136-44. Accessed March 31, 2005. doi: 10.1016/j.jallcom.2005.03.053.

Lee, HaYong, Jung, SeHun, Lee, SooYong, and Ko, KyungHyun. "Fabrication of Cold Sprayed Al-Intermetallic Compounds Coatings by Post Annealing." Materials Science and Engineering A 433 (2006): 139-43. Accessed June 17, 2007. doi: 10.1016/j.msea.2006.06.044.

Lee, HaYong, Lee, SoYong, and Ko, KyungHyun. "Annealing Effects on the Intermetallic Compound Formation of Cold Sprayed Ni, Al Coatings." Journal of Materials Processing Technology 209 (2009): 937-43. Accessed March 2, 2008. doi: 10.1016/.jmatprotec. 2008.03.001.

Lee, HaYong, and Ko, KyungHyun. "Effect of SiC Particle Size on Cold Sprayed Al-SiC Composite Coatings." Surface Engineering 25 (2009): 606-11. Accessed July 2, 2007. doi: 10.1179/174329408X271516.

Lee, HaYong, Lee, SoYong, Shin, HeeJae, and Ko, KyungHyun. "Mechanical Matching and Microstructural Evolution at the Coating/Substrate Interfaces of Cold-Sprayed Ni, Al coatings." Journal of Alloys and Compounds 478 (2009): 636-41. Accessed November 21, 2008. doi: 10.1016/j.jallcom.2008.11.150.

Lee, HaYong, and Ko, KyungHyun. "Fabrication of Porous Al Alloy Coatings by Cold Gas Dynamic Spray Process." Surface Engineering 26 (2010): 395-8. Accessed July 22, 2009. doi: 10.1179/026708409X12490360426124.

Li, Jianfeng, Agyakwa, Pearl A., Johnson, Carole Mark, Zhang, Deen, Hyssain, Tanvir, and McCartney, David Graham. "Characterization and Solderability of Cold Sprayed Sn Cu Coatings on Al and Cu Substrates." Surface and Coatings Technology 204 (2010): 1395-404. Accessed September 9, 2009. doi:10.1016/j.surfcoat. 2009.09.025.

Li, WenYing, Zhang, Chao, Guo, Xyeping, Zhang, Ga, Liao, Hanlin, and Coddet, Christian. "Deposition Characteristics of Al-12Si Alloy Coating Fabricated by Cold Spraying with Relatively Large Powder Particles." Applied Surface Science 253 (2007): 7124-30. Accessed February 2, 2007. doi: 10.1016/j.apsusc.2007.02.142.

Li, WenYing, Zhang, Ga, Liao, Hanlin, and Coddet, Christian. "Characterizations of Cold Sprayed TiN Particle Reinforced Al2319 Composite Coating." Journal of Materials Processing Technology 202 (2008): 508-13. Accessed September 19, 2007. doi: 10.1016/j.jmatprotec. 2007.09.045.

Ma, Xin, Wang, Fengjiang, Qian, Yiyu, and Yoshida, Fusahito. "Development of Cu-Sn Intermetallic Compound at Pb-Free Solder-Cu Joint Interface." Materials Letters 57 (2003): 3361-5. Accessed January 20, 2003. doi: 10.1016/S0167-577X(03)00075-2.

Ning, Xian-Jin, Kim, JinHong, Kim, HyungJun, and Lee, Changhee. "Characteristics and Heat Treatment of Cold-Sprayed Al-Sn Binary Alloy Coatings." Applied Surface Science 255 (2009): 3933-9. Accessed October 10, 2008. doi: 10.1016/j.apsusc.2008.10.074.

Novoselova, Tatiana, Fox, Peter, Morgan, Rhys H., and O'Neill, William "Experimental Study of Titanium/Aluminium Deposits Produced by Cold Gas Dynamic Spray." Surface and Coatings Technology 200 (2006): 2775-83. Accessed October 28, 2004. doi: 10.1016/j.surfcoat.2004.10.133.

Peng, Ming, and Mikula, Adolf. "Thermodynamic Properties of Liquid Cu-Sn-Zn Alloys." Journal of Alloys and Compounds 247 (1997): 185-9. Accessed January, 1997. doi: 10.1016/S0925-8388(96)02575-3.

Spencer, Kevin K., and Zhang, Mingxing. "Heat Treatment of Cold Spray Coatings to Form Protective Intermetallic Layers." Scripta Materialia 61 (2009): 44-7. Accessed March 3, 2009. doi: 10.1016/j.scriptamat. 2009.03.002.

Tao, Yongshan, Xiong, Tianying, Sun, Chao, Jin, Huazi, Du, Hao, and Li, Tiefan. "Effect of α-Al2O3 on the Properties of Cold Sprayed Al/α-Al2O3 Composite Coatings on AZ91D Magnesium Alloy." Applied Surface Science 256 (2009): 261-6. Accessed August 3, 2009. doi: 10.1016/j.apsusc.2009.08.012.

Villafuerte, Julio C. "Recent Trends in Cold Spray Technology: Looking at the Future." Surface Engineering 26 (2010): 393-4. Accessed August 1, 2010. doi: 10.1179/026708410X12687356948715.

Wang, HongTao, Li, ChangJiu, Yang, GuanJun, and Li, ChengXing. "Cold Spraying of Fe/Al Powder Mixture: Coating Characteristics and Influence of Heat Treatment

on the Phase Structure." Applied Surface Science 255 (2008): 2538-44. Accessed July 22, 2008. doi: 10.1016/j.apsusc.2008.07.127.

Wielage, Bernhard, Podlesak, Harry, Grund, Thomas, and Wank, Andreas, Chemnitz/D. "Cold Gas Sprayed Filler Coatings for Brazing Of Light Alloys." Surface Engineering 115 (2006): 98-102. Accessed April, 2006. doi: 10.1179/174329406X98386.

Wielage, Bernhard, Grund, Thomas, Rupprecht, Christian, and Kuemmel, S. "New Method for Producing Power Electronic Circuit Boards by Cold-Gas Spraying and Investigation of Adhesion Mechanisms." Surface and Coatings Technology 205 (2010): 1115-8. Accessed June 21, 2010. doi: 10.1016/j.surfcoat. 2010.06.020.

Yu, Daquan, Zhao, Zongbin, and Wang, LaiGui. "Improvement on the Microstructure Stability, Mechanical and Wetting Properties of Sn-Ag-Cu Lead-Free Solder with the Addition of Rare Earth Elements." Journal of Alloys and Compounds 376 (2004): 170-5. Accessed January 8, 2004. doi: 10.1016/j.jallcom. 2004.01.012.

Zou, Hefei, Yang, Huajie, and Zhang, Zhefeng. "Coarsening Mechanisms, Texture Evolution and Size Distribution of Cu_6Sn_5 between Cu and Sn-Based Solders." Materials Chemistry and Physics 131 (2011): 190-8. Accessed August 26, 2011. doi: 10.1016 /j.matchemphys. 2011.08.061.
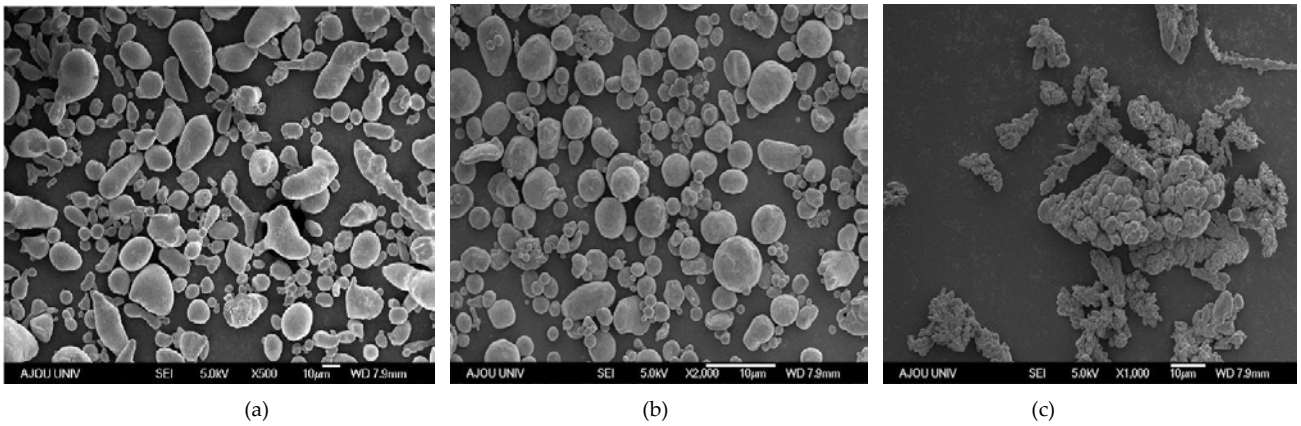
(a)   (b)   (c)

FIG. 1 SEM IMAGES OF THE AS-PURCHASED CU AND SN POWDERS USED IN THE EXPERIMENT:
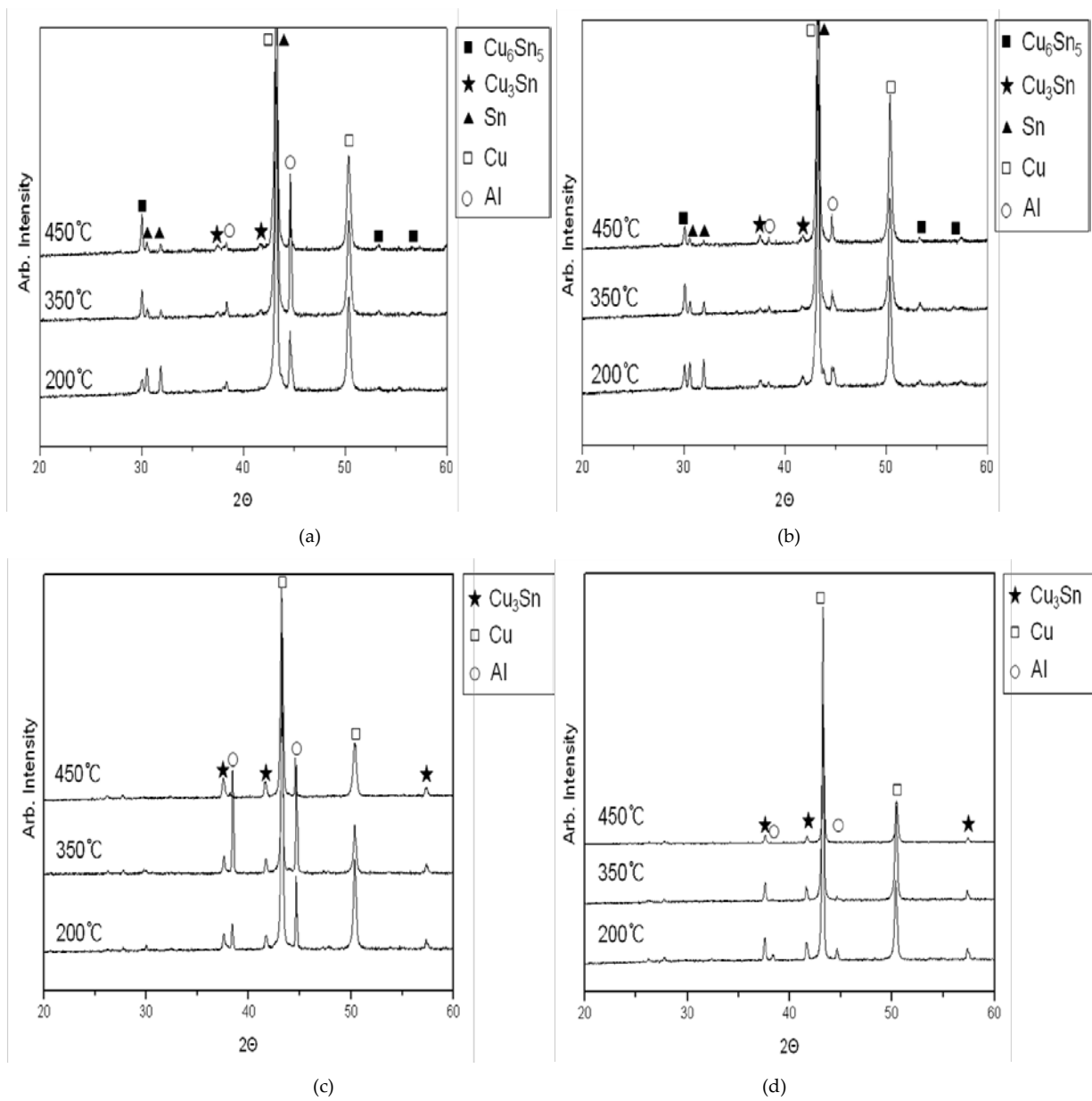
Cu (10 μm), (b) Cu (44 μm), AND (c) Sn POWDERS (44 μm).

(a)   (b)

(c)   (d)

FIG. 2 XRD PATTERNS OF CU-SN COMPOSITE COATINGS:

(a)   AS-COATED Cu (10 μm)-Sn, (b) AS-COATED Cu (44 μm)-Sn, (c) ANNEALED Cu (10 μm)-Sn, AND (d) ANNEALED Cu (44 μm)-Sn.

<center>(a)</center>

<center>(b)</center>

<center>(c)</center>

<center>(d)</center>

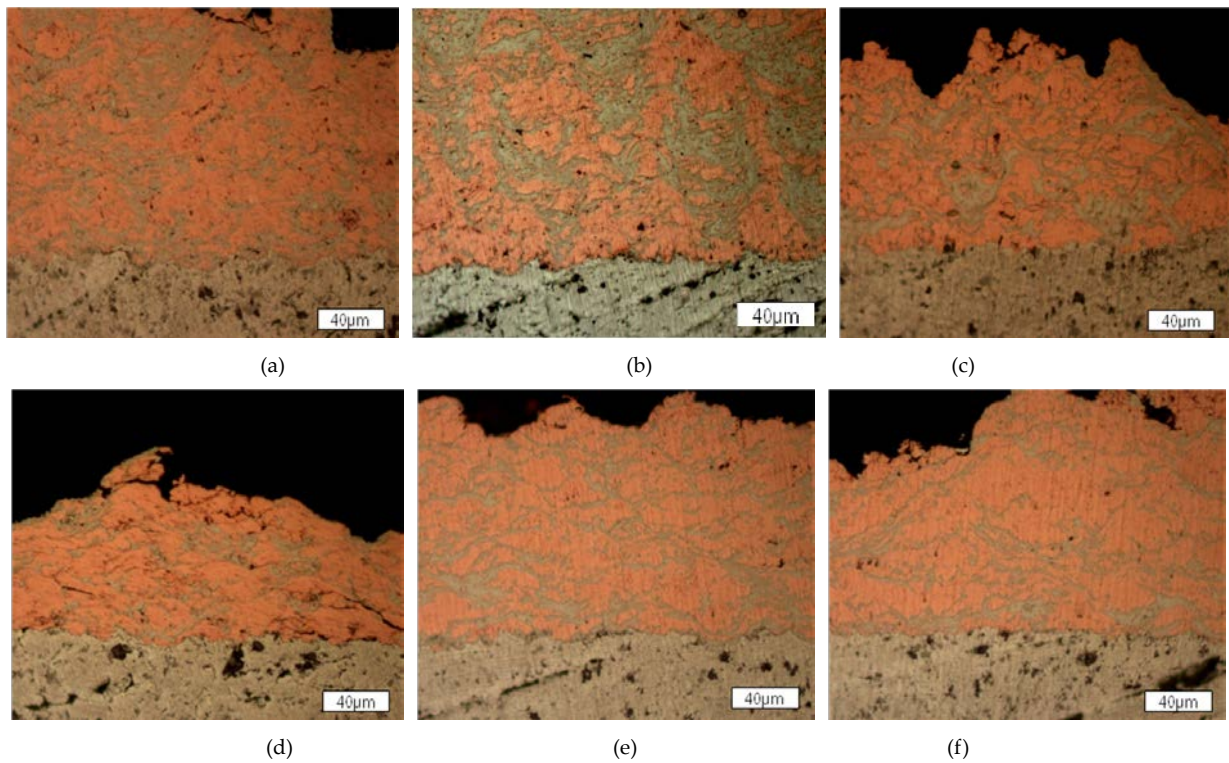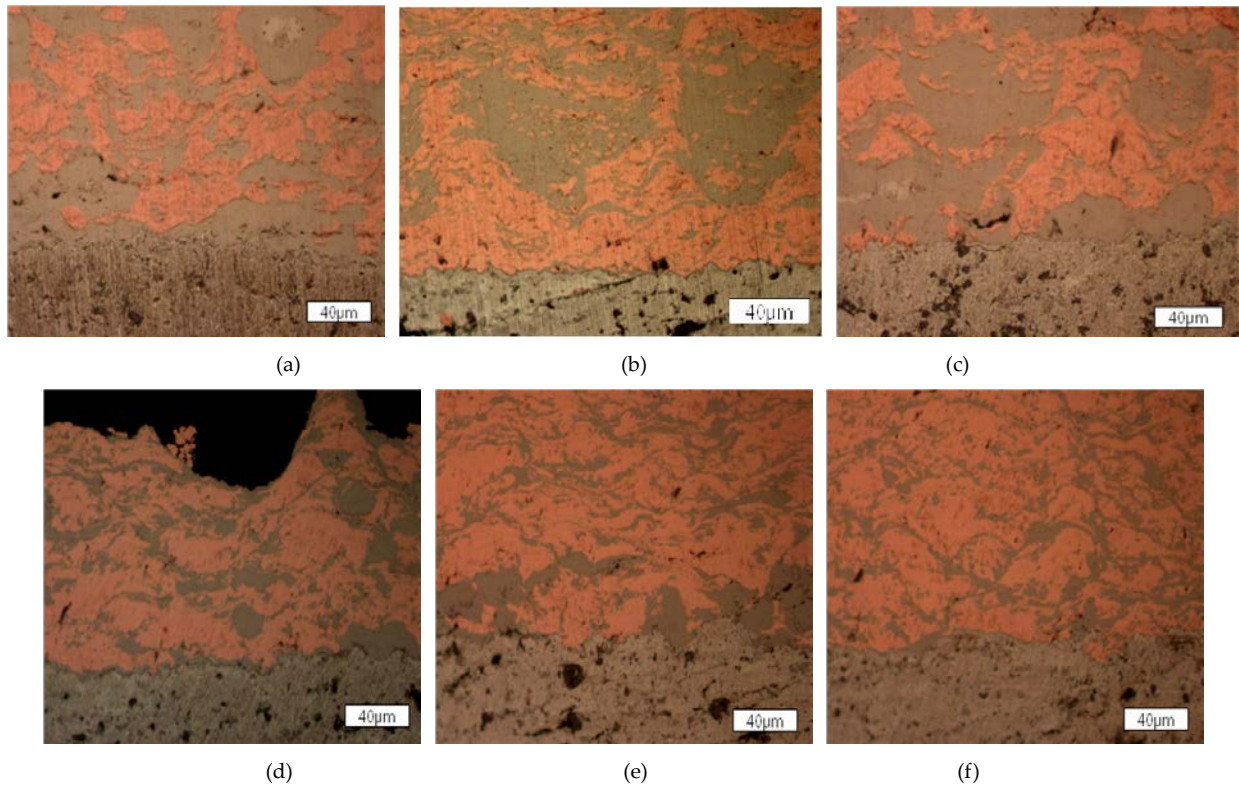<center>(e)</center>

<center>(f)</center>

FIG. 3 POLISHED CROSS-SECTION IMAGES (OM) OF AS-COATED CU-SN COMPOSITE COATINGS WITH RESPECT TO TYPE OF CU POWDER AND GAS TEMPERATURE CONDITIONS:

(a) Cu (10 μm)-Sn, 200ºC, (b) Cu (10 μm)-Sn, 350ºC, (c) Cu (10 μm)-Sn, 450ºC, (d) Cu (44 μm)-Sn, 200ºC, (e) Cu (44 μm)-Sn, 350ºC, AND (f) Cu (44 μm)-Sn, 450ºC.

<center>(a)</center>

<center>(b)</center>

<center>(c)</center>

<center>(d)</center>

<center>(e)</center>

<center>(f)</center>

FIG. 4 POLISHED CROSS-SECTION IMAGES (OM) OF ANNEALED CU-SN COMPOSITE COATINGS WITH RESPECT TO TYPE OF CU POWDER AND GAS TEMPERATURE CONDITIONS:

(a) Cu (10 μm)-Sn, 200ºC, (b) Cu (10 μm)-Sn, 350ºC, (c) Cu (10 μm)-Sn, 450ºC, (d) Cu (44 μm)-Sn, 200ºC, (e) Cu (44 μm)-Sn, 350ºC, AND (f) Cu (44 μm)-Sn, 450ºC.
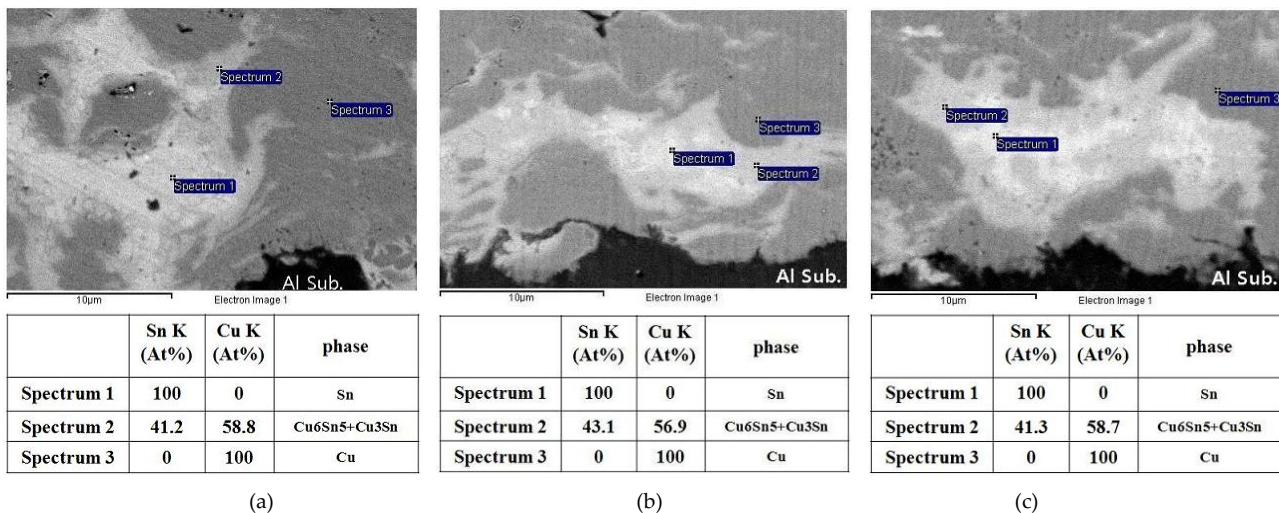
	Sn K (At%)	Cu K (At%)	phase
Spectrum 1	100	0	Sn
Spectrum 2	41.2	58.8	Cu6Sn5+Cu3Sn
Spectrum 3	0	100	Cu

(a)

	Sn K (At%)	Cu K (At%)	phase
Spectrum 1	100	0	Sn
Spectrum 2	43.1	56.9	Cu6Sn5+Cu3Sn
Spectrum 3	0	100	Cu

(b)

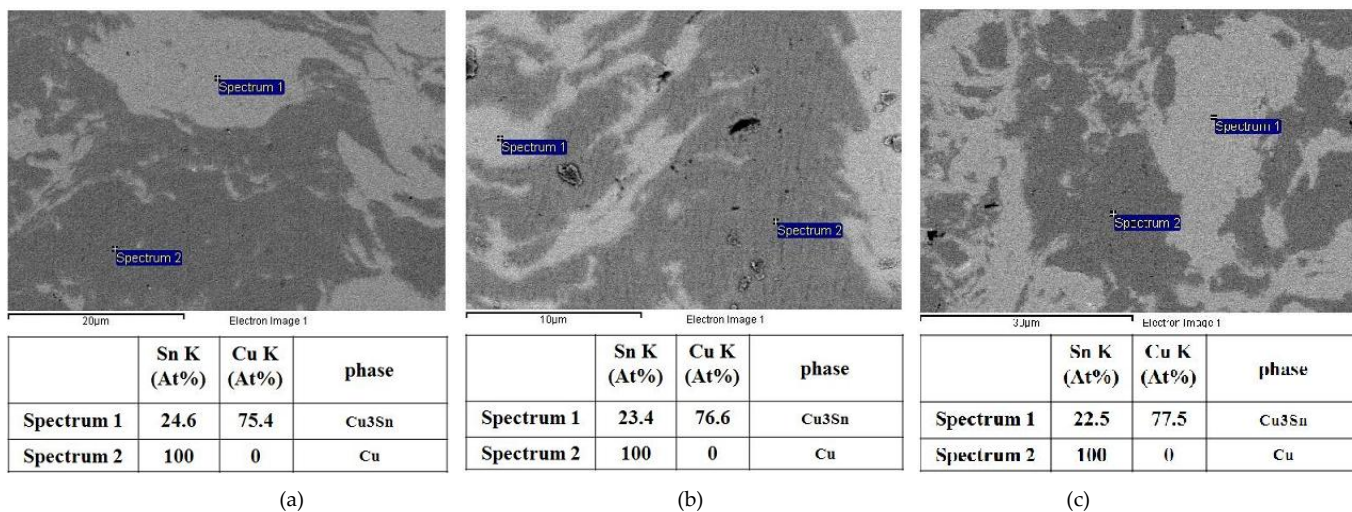|	Sn K (At%)	Cu K (At%)	phase
Spectrum 1	100	0	Sn
Spectrum 2	41.3	58.7	Cu6Sn5+Cu3Sn
Spectrum 3	0	100	Cu

(c)

FIG. 5 THE BACKSCATTERED ELECTRON IMAGES OF AS-COATED CU (10 MM)-SN COMPOSITE COATINGS USING FESEM WITH EDS: AT A GAS TEMPERATURE OF (a) 200ºC, (b) 300ºC, OR (c) 450ºC.
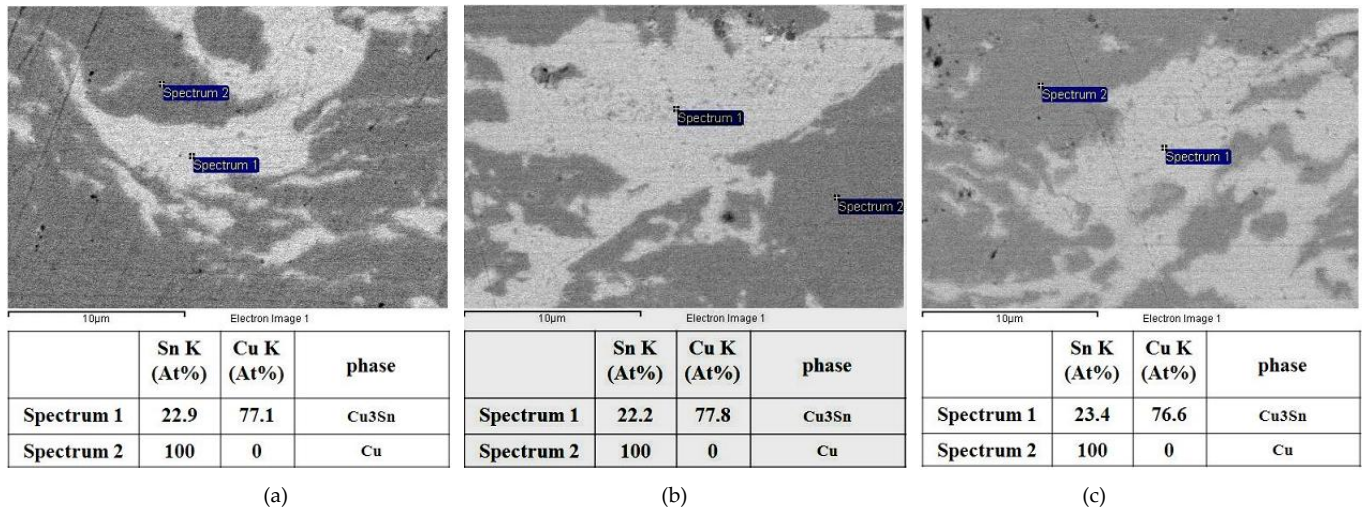

	Sn K (At%)	Cu K (At%)	phase
Spectrum 1	100	0	Sn
Spectrum 2	39.3	60.7	Cu6Sn5+Cu3Sn
Spectrum 3	0	100	Cu

(a)

	Sn K (At%)	Cu K (At%)	phase
Spectrum 1	100	0	Sn
Spectrum 2	41.5	58.5	Cu6Sn5+Cu3Sn
Spectrum 3	0	100	Cu

(b)

	Sn K (At%)	Cu K (At%)	phase
Spectrum 1	100	0	Sn
Spectrum 2	41.8	58.3	Cu6Sn5+Cu3Sn
Spectrum 3	0	100	Cu

(c)
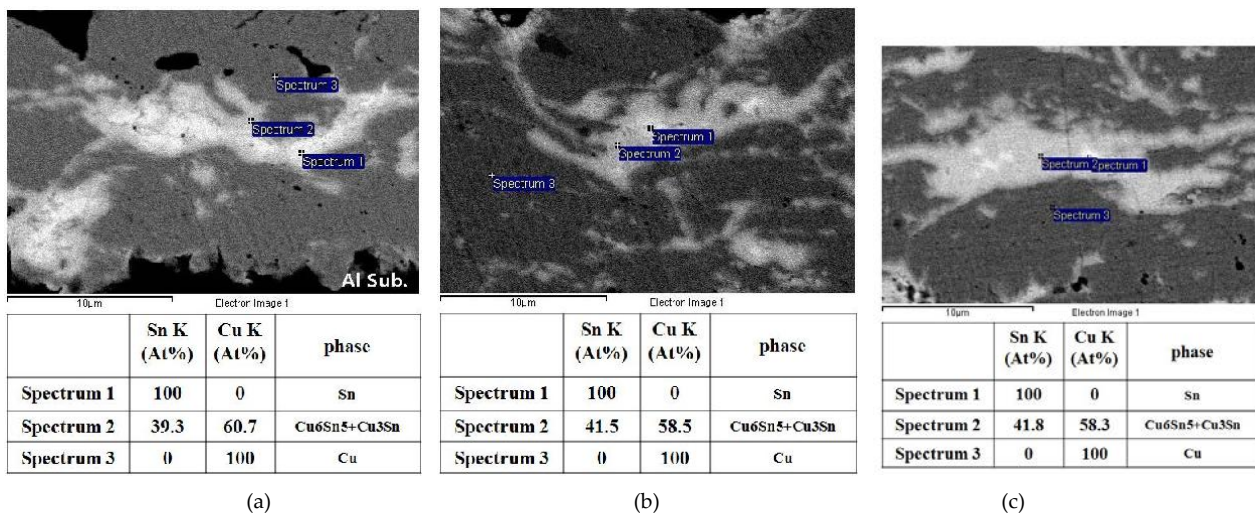
FIG. 6 THE BACKSCATTERED ELECTRON IMAGES OF AS-COATED CU (44 MM)-SN COMPOSITE COATINGS USING FESEM WITH EDS: AT A GAS TEMPERATURE OF (a) 200ºC, (b) 300ºC, (c) 450ºC.


	Sn K (At%)	Cu K (At%)	phase
Spectrum 1	24.6	75.4	Cu3Sn
Spectrum 2	100	0	Cu

(a)

	Sn K (At%)	Cu K (At%)	phase
Spectrum 1	23.4	76.6	Cu3Sn
Spectrum 2	100	0	Cu

(b)

	Sn K (At%)	Cu K (At%)	phase
Spectrum 1	22.5	77.5	Cu3Sn
Spectrum 2	100	0	Cu

(c)

FIG. 7 THE BACKSCATTERED ELECTRON IMAGES OF ANNEALED CU (10 MM)-SN COMPOSITE COATINGS USING FESEM WITH EDS: AT A GAS TEMPERATURE OF (a) 200ºC, (b) 300ºC, OR (c) 450ºC.

	Sn K (At%)	Cu K (At%)	phase
Spectrum 1	22.9	77.1	Cu3Sn
Spectrum 2	100	0	Cu

(a)

	Sn K (At%)	Cu K (At%)	phase
Spectrum 1	22.2	77.8	Cu3Sn
Spectrum 2	100	0	Cu

(b)

	Sn K (At%)	Cu K (At%)	phase
Spectrum 1	23.4	76.6	Cu3Sn
Spectrum 2	100	0	Cu

(c)

FIG. 8 THE BACKSCATTERED ELECTRON IMAGES OF ANNEALED CU (44 MM)-SN COMPOSITE COATINGS USING FESEM WITH EDS:

AT A GAS TEMPERATURE OF (a) 200ºC, (b) 300ºC, OR (c) 450ºC.

(a)   (b)
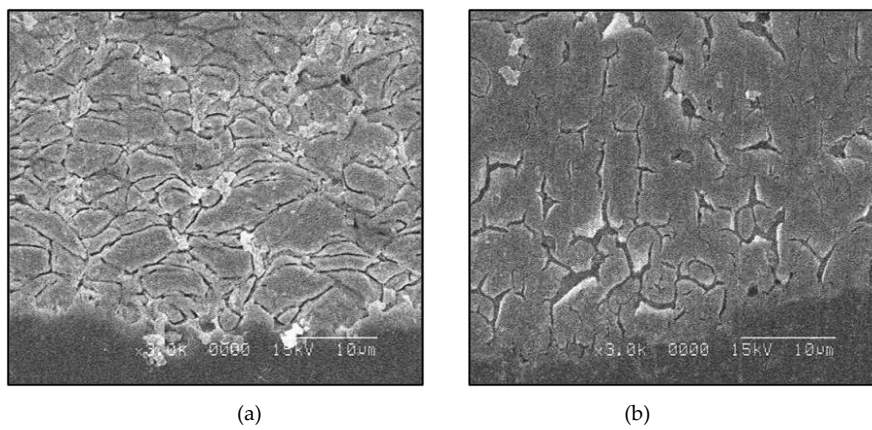
FIG. 9 CROSS-SECTION IMAGES (SEM) OF PURE CU COATINGS USING DIFFERENT CU POWDERS:

(a) 10 μm, (b) 44 μm.

Respirometric Evaluation of the Biodegradability of Films of PE/PHBV Blends

S. P. C. Gonçalves[*1], S. M. Martins-Franchetti[2]

Biochemistry and Microbiology Department, UNESP

Av 24A, 1515 – Rio Claro/SP Brazil

[*1]spcgon@rc.unesp.br; [2]samaramf@rc.unesp.br

Abstract

Films of Polyethylene (PE), Poly (3-hydroxybutyrate-co-hydroxyvalerate) (PHBV, 18% HV) and PE/PHBV blends containing 10 and 30% of PHBV were buried in soil for 180 days to evaluate their biodegradability through the respirometry test. The biodegradation of the films was investigated by Fourier transform infrared spectroscopy (FTIR), X-ray diffraction (XRD) and scanning electron microscopy (SEM). The biodegradation rate was found to be increased in blends containing larger proportions of biodegradable polymer, due to increasing interphase (intermediate regions) between the two polymers. Therefore, the biodegradation rate was proportional to the amount of biodegradable polymer phase (PHBV) in contact with the PE.

Keywords

Biodegradation; PE; PHBV

Introduction

The extensive and increasing use of polymer materials with their wide range of applications in various areas has created a significant rise in plastic waste discarded in the environment, encouraging the scientific community to investigate new polymer materials, such as blends between degradable and synthetic polymers [Rosa 2009, Gonçalves 2009, Santana 2012, Campos 2010, Shah 2008, Luckachan 2011].

Polyethylene (PE) is a synthetic polymer widely used on a commercial scale, especially in the packaging industry due to its easy production, excellent chemical resistance and processability [Kyrikou 2011]. After used up, PE materials are discarded into different ecosystems, where they cause numerous problems associated with the accumulation of solid waste due to their inertia and resistance to microorganisms.

One option to reduce the accumulation of solid waste is the use of biodegradable polymers that are accessible to microbial assimilation. Polyhydroxyalkanoates (PHAs), whose mechanical and thermal properties are similar to those of conventional thermoplastics, are polyesters produced in nature by bacteria. A representative the family of PHAs is Poly (3-hydroxybutyrate-co-hydroxyvalerate) (PHBV), whose desirable mechanical performance and rapid biodegradation in different natural environments make it an attractive material [Hermida 2009].

The biodegradation of polymers is influenced by their chemical structure, especially the presence of functional groups, their hydrophobic-hydrophilic balance, the presence of highly ordered structures such as crystallinity and orientation, and other morphological properties [Oldak 2005, Gu 2003]. Most of the tests employed to monitor polymer biodegradation are based on the determination of CO_2 produced by microbial respiration [Calmon 2000, Krzan 2006, Bastioli 2005], combined with measures of structural changes (FTIR) and morphology (XRD) of polymers [Starka 2004, Furukawa 2007, Conti 2006, Kunioka 1989].

The polymer blends obtained by mixing synthetic and biodegradable polymers can allow for good interaction with microorganisms in the environment. This study investigated the biodegradation of PE/PHBV blends containing 10 and 30% PHBV, based on respirometric tests, FTIR, XRD and SEM.

Materials and Methods

The polymers used in this study were LDPE with a density of 0.922 g/cm³ and MFI (melt flow index) of 3.8 g/10 min (Braskem PE BP-681/59) and PHBV (Mw = 237,500, 18 mol% HV content).

The polymers and blends were mixed for 15 min in a Thermo Haake rheometer operated at 170°C and 60 rpm. The polymer films were compression-molded for 3 min at 170°C between two aluminum sheets in a hot hydraulic press, under a pressure of 8.7 MPa to obtain 100 μm thick films. The films were then allowed to

cool to ambient temperature (25-26°C).

The polymer films were subjected to respirometry testing to quantify the production of carbon dioxide released by microbial respiration and to evaluate their biodegradation, according to the ISO 14855 standard [Weng 2011]. Biometer flasks used as originally suggested by Bartha and Pramer [Bartha 1965], each containing 50 g of soil + polymer sample (duplicate) were incubated at 28°C ± 2°C for 180 days. CO_2 production was measured volumetrically at intervals of approximately 24 h.

Infrared spectra of the blend and pure films were recorded in a Shimadzu Prestige-21 FTIR spectrometer operated at a spectral resolution of 4 cm^{-1} for all the samples, with scanning performed at room temperature before and after the respirometric test.

X-ray diffraction (XRD) measurements were taken using a RIGAKU RU-200B diffractometer (belonging to IFSC/USP, São Carlos, SP, Brazil) operated at 50 kV and 100 mA using a CuKα radiation wavelength of 1.54 A as the X-ray source. Diffraction patterns were recorded in the range of 2θ = 10–35° at a scan speed of 0.36°/min at room temperature.

The changes occurring on the surface of the polymer films were analyzed under a Zeiss DSM 940-A scanning electron microscope, using an acceleration voltage of 4 keV.

Results

A respirometer is used to measure the volume of CO_2 produced by the respiration of microorganisms during aerobic biodegradation [Kijchavengkul 2006]. The evolution of CO_2, a direct parameter to verify polymer mineralization, is therefore a useful way to determine the biodegradability of polymer material [Calmon 2000, Bastioli 2005, Solaro 1998].

Fig. 1 shows the percentage of biodegradation of polymer films based on CO_2 production. PHBV films incubated for 6 months presented the highest biodegradation rate, which was evidenced by the impossibility to detect the films in the soil after this experimental period due their complete disintegration. The PHBV films became mineralized by the action of the microorganisms in the soil. This was demonstrated earlier by Weng et al. [Weng 2011] who studied the biodegradation of PHAs (PHB, PHBV (40, 20 and 3 mol% HV) and P(3HB, 4HB) (10% mol 4HB) under controlled composting conditions, and found that 50% of the films were undetectable after 20 days due to

their biodegradation by enzyme catalyzed erosion occurring from the surface toward the core of the films.
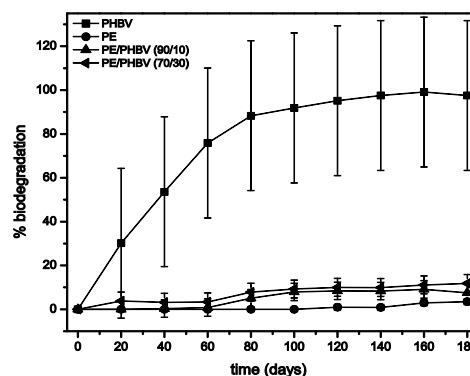

FIG. 1 PERCENTAGE OF FILMS BIODEGRADATION FROM RESPIROMETRY ANALYSIS, WITH AVERAGE STANDARD DEVIATION.

In this work, the PE films started to biodegrade after 120 days, keeping about 3.5% of biodegradation at the end of the experiment. The long period of latency is attributed to the properties of the material, such as hydrophobicity and degree of crystallinity [Roy 2008] which are important factors in biodegradation due to the effect of water and enzyme accessibility [Vilaplana 2010]. Corti et al. [2010] found that the production of CO_2 in preoxidized PE samples containing prooxidant additives was greater than that in films without these additives. This finding was explained by the ability of fungi to use the products of oxidation as sources of carbon.

The PE/PHBV 90/10 and 70/30 blends showed 7 and 12% biodegradation, respectively, in the same period, with greater biodegradation of the blend containing the higher proportion of biodegradable polymer (70/30).

CO_2 evolution, an efficient method to assess the biodegradation of polymer films, is directly related with the morphology of biodegraded polymer films, as illustrated in the following FTIR, XRD and SEM images.

Infrared spectroscopy is a versatile technique to determine compositions and macromolecular configurations, and to compare morphologies against parameters such as crystallinity (crystallinity index) and phase segregation of polymer systems [Gulmine 2002, Sato 2011]. However, the crystallinity index does not represent an absolute degree of crystallinity [Bloembergen 1986].

Fig. 2 shows FTIR spectra of the untreated PHBV and

biotreated films. The spectra were normalized using the band at 1380 cm^{-1} as internal standard, which is assigned to CH$_3$ symmetric deformation, independent of crystallinity [Singh 2008]. The spectra of the PE and blend films after 180 days of biotreatment were normalized in relation to the band at 1465 cm^{-1} (CH$_2$) [Sudhakar 2008].

After the respirometric test, the PE showed 8% increase in the intensity of the band at 1377 cm^{-1}, which was attributed to the percentage of short chain branching (methyl, butyl and hexyl) of the PE bonds, indicating breaks in these chains [Quental 2005].

After the respirometric test on the PHBV and blends, several changes were detected in the bands at 1278 and 1184 cm^{-1} which were attributed, respectively, to CH$_2$ vibrations and C-O-C stretching in the amorphous phase, emphasizing that these bands are sensitive to the crystallinity of PHB [Furukawa 2007, Bloembergen 1986, Bayari 2005]. In addition, the intensity of the band at 1722 cm^{-1} was found to increase (C=O in crystalline phase). Before the respirometry test, the 90/10 blend showed a band at 1735 cm^{-1}, which was assigned to C=O in a less organized crystalline phase [Conti 2006, Padermshoke 2005]. This phase underwent changes after the biotreatment, suggesting hydrolytic breaks of ester groups of the PHB fraction and some chain rearrangements. In the biotreated 70/30 blend, the band at 1742 cm^{-1} (C=O amorphous phase) was found to be absent, indicating consumption of carbonyl and consequent chain rearrangements of PHBV in contact with PE phase.
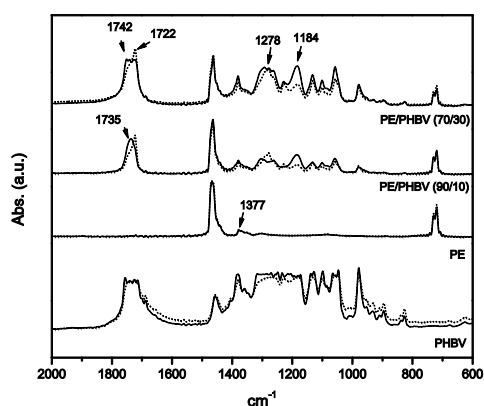

FIG. 2 FTIR OF THE FILMS BEFORE AND AFTER THE RESPIROMETRIC ASSAY.

The degree of crystallinity (% Xc) and the crystallite size (D) were calculated from XRD data extracted from Fig. 3. Crystallinity was calculated based on the ratio of crystalline to amorphous peak areas. Crystallite size was calculated using Scherrer's equation [Munaro 2008], where B is the width at half height of the highest peak, θ is its angle position; k is a constant, which depends on particle size (spherical shape = 0.9) and λ is the X-ray length (Table 1).

The principal reflection peaks in the PHBV were at 2θ = 13.30 and 16.68°, corresponding to the (110) and (020) planes, emphasizing that the PHB (polyhydroxybutyrate) plane (110) also occurs at 2θ ~ 16.8°. The PE planes (110) and (200) are located at 2θ = 21.36 and 23.62°, respectively.

After the biotreatment, the crystallite size (D) of the blends underwent modifications in the 110 plane, relative to the PHBV and PE fractions. In the PHBV fraction, the crystallite size decreased by about 7.5% in the 90/10 blend, due to the greater dispersion of PHBV domains in the PE matrix. However, in the 70/30 blend, the crystallite size of PHBV increased by 15%, because of the greater coalescence of the PHBV domains. The crystallite size in the PE fraction of the 90/10 and 70/30 blends increased by about 4.5% and 1.5%, respectively (Table 1), suggesting that in the blend containing the larger amount of synthetic polymer (PE), these chains underwent new crystallization on pre-existing crystals [Gonçalves 2009, Guadagno 2001]. The crystallite size in the biotreated PE showed a 2% decrease and the PHBV a 44% increase.

The degree of crystallinity (Xc) of PHBV decreased significantly (22 %) after 28 days buried in the soil, but increased by about 4% in PE after 180 days. The 90/10 blend showed an increase (8%) similar to that found in the PE films. The biotreated 70/30 blend showed an 8% decrease in Xc due to degradation of the PHBV crystalline fraction, represented by the (110) peak, which was assigned to HV chains.

The changes in the crystallite size of the PHBV and the 70/30 blend after the respirometric assay probably occurred due to biodegradation of the HV (valerate) chains, which caused the crystallite size to increase. Following Yoshie et al.'s model [2001], which proposes that PHBV is isodimorphic, i.e., the long sequences of HB (butyrate) units comprise the crystal core and the HV units comprise edges of the lamella, where the biodegradation process occurs. In the 70/30 blend, the larger and less organized interphases composed of flexible valerate units enable the biodegradation reactions. This was confirmed by the FTIR results, especially by the PHB bands sensitive to the degree of crystallinity, which underwent changes.
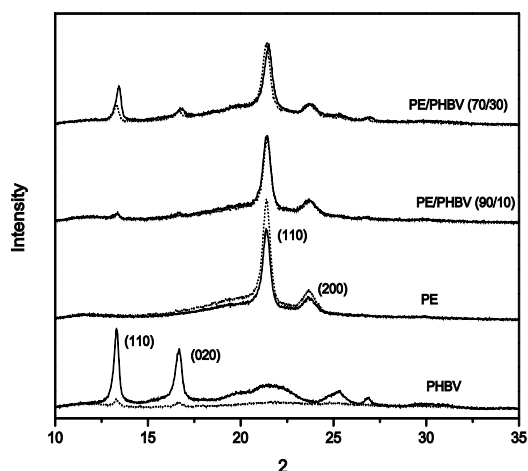
the 70/30 blend.

FIG. 3 XRD OF THE FILMS BEFORE AND AFTER THE RESPIROMETRIC ASSAY.

As shown in Fig. 2 (FTIR), branching PE presented a band relative to the short chains (methyl, ethyl, butyl). This PE underwent a break of the C-C and C-H bonds, which was facilitated by tertiary carbon, producing short chains after degradation [Corrales 2002]. In this experiment, PE began to biodegrade at around 120 days (respirometry data), suggesting that biodegradation started from the breaking of these weak bonds around the tertiary carbon, mainly in the amorphous phase, as reported in the literature [Volke-Sepulveda 2002, Suresh 2011]. In the 90/10 blend, which showed greater dispersion of PHBV in the PE matrix and smaller domains of PHBV, the degree of biodegradation was less (FTIR and XRD results).

TABLE 1 - CRYSTALLITES SIZE (D) AND CRYSTALLINITY DEGREE (%XC) TO THE FILMS BEFORE AND AFTER THE RESPIROMETRIC ASSAY.

samples	D (nm) (110) PHBV		D (nm) (110) PE		% Xc	
	before	after	before	after	before	after
PHBV	4.2845	6.1802	---	---	60	47
PE	---	---	3.1373	3.0826	54	56
90/10	6.2920	5.8202	2.9977	3.1377	47	51
70/30	4.2851	4.9180	3.0369	3.0963	52	48

Fig. 4 shows micrographs of the films before and after the respirometric assay. The original films showed smooth surfaces (Fig. 4 a,c,e,g,i). After 28 days, the PHBV films showed craters and erosion on all the surfaces (Fig. 4 b). After 180 days of biotreatment, the PE films and blends displayed a few changes, such as grooving and exfoliation of surface layers, mainly in
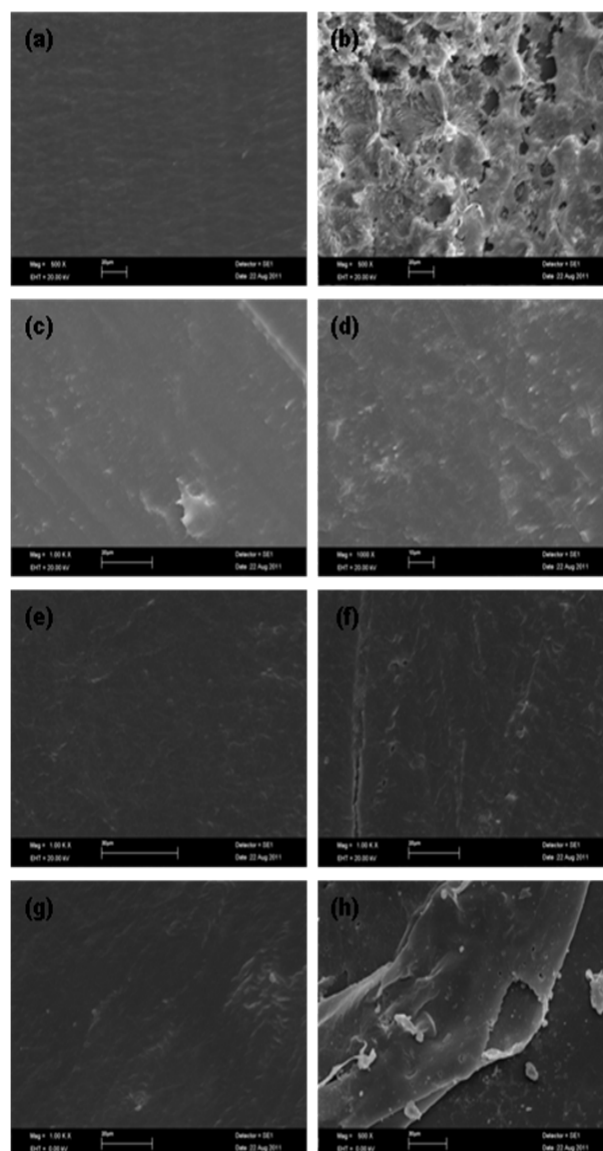

FIG. 4 FILMS SEM (A) PHBV BEFORE THE RESPIROMETRIC ASSAY; (B) PHBV AFTER 28 DAYS; (C) PE BEFORE; (D) PE AFTER 180 DAYS; (E) PE/PHBV 90/10 BEFORE; (F) PE/PHBV 90/10 AFTER; (G) PE/PHBV 70/30 BEFORE; (H) PE/PHBV 70/30 AFTER 180 DAYS.

The results of the biodegradation of blends indicated that the larger the proportion of biodegradable polymer was, the higher the biodegradation rate was. Thus, a large amount of PHBV results in a phase with larger domains of PHBV (more clusters), similar to what Oldak et al. [2005] found in their study who studied photodegradation and biodegradation of PE/cellulose blends, and concluded that blends with a higher proportion of cellulose (30%) formed larger domains, so that the interactions were not strong enough to prevent their degradation. In the 5-15% PE/cellulose blend, the cellulose disperses more homogeneously, with short inclusions in the PE matrix, facilitating the intermolecular interactions and

hindering biodegradation. This effect was reported by Borah & Chaki [2011] who used a blend of low density polyethylene/methyl ethylene-co-acrylate and found two phases, with the minor component (cellulose) dispersed in the main continuous matrix (PE).

Thus, in the present study, the higher the proportion of PHB in the blend was, the larger the interphase between the polymers was, which was considered an intermediate and less organized phase where biodegradation occurred preferentially. The changes observed in PHBV and PE/PHBV blends were attributed to the action of microorganisms that catalyzed hydrolytic reactions of PHBV ester groups at the interface between crystalline and amorphous phases (in PHBV) and in interphases (intermediate regions between PE and PHBV in the blend). Hence, the larger the interphase was, the greater the probability of the occurrence of biodegradation was (as in the case of the 70/30 blend).

Conclusions

Blends containing higher proportions of PHBV showed higher susceptibility to microbial degradation in soil, due to the distribution of the larger phases (PHBV) in contact with the PE matrix (interphase). The samples biodegraded in the following sequence: PHBV > PE/PHBV 70/30 > PE/PHBV 90/10 > PE.

The microbial action occurred through the hydrolysis of PHBV ester groups (at the interface between amorphous and crystalline phases) and in interphases in the blend (contact between the two different polymers).

CO_2 evolution (respirometry) is an efficient method to assess the biodegradation of polymer films, particularly when allied to FTIR, XRD and SEM techniques.

REFERENCES

Adelman, Rachel. "'Such Stuff as Dreams Are Made On': God's Footstool in the Aramaic Targumim and Midrashic Tradition." Paper presented at the annual meeting for the Society of Biblical Literature, New Orleans, Louisiana. November 21–24, 2009.

Bartha, R.; Pramer, D. "Features of a Flask and Method for Measuring the Persistence and Biological Effects of Pesticides in Soil", Soil Science 100 (1965): 68 – 70.

Bastioli, C. Handbook of Biodegradable Polymers, Rapra Technology Limited, 2005.

Bayari, S.; Severcan, F. "FTIR Study of Biodegradable Biopolymers: P(3HB), P(3HB-co-4HB) and P(3HB-co-3HV)", Journal of Molecular Structure 744–747 (2005): 529–534.

Bloembergen, S.; Holden, D. A.; Hamer, G. K.; Bluhm, T. L.; Marchessault, R. H. "Studies of Composition and Crystallinity of Bacterial Poly(β-hydroxybutyrate-co-β-hydroxyvalerate)", Macromolecules 19 (1986): 2865-2871.

Borah, J. S.; Chaki, T. K. "Dynamic Mechanical, Thermal, Physico-Mechanical and morphological Properties of LLDPE/EMA blends", J Polym Res 18 (2011): 569–578.

Calmon, A.; Bresson, L. D.; Maurel, V. B.; Feuilloley, P.; Silvestre, F. "An Automated Test for measuring Polymer Biodegradation", Chemosphere 41 (2000): 645-651.

Campos, A.; Marconato, J. C.; Franchetti, S. M. M. "Biodegradação de filmes de PP/PCL em Solo E Solo Com Chorume", Polímeros Ciência e Tecnologia 20 (2010): 295-300.

Conti, D.S.; Yoshida, M.I.; Pezzin, S.H.; Coelho, L.A.F. "Miscibility and Crystallinity of Poly(3-Hydroxybutyrate)/Poly(3-Hydroxybutyrate-Co-3-Hydroxyvalerate) blends", Thermochimica Acta 450 (2006): 61–66.

Corrales, T.; Catalina, F.; Peinado, C.; Allen, N.S.; Fontan, E. "Photooxidative and Thermal Degradation of Polyethylenes: Interrelationship by Chemiluminescence, Thermal Gravimetric Analysis and FTIR Data", J Photochem Photobiol A: Chemistry 147 (2002): 213–224.

Corti, A.; Muniyasamy, S.; Vitali, M.; Imamc, S. H.; Chiellini, E. "Oxidation and Biodegradation of Polyethylene Films Containing Pro-Oxidant Additives: Synergistic Effects of Sunlight Exposure, Thermal Aging and Fungal Biodegradation", Polym Degrad Stab 95 (2010): 1106-1114.

Furukawa, T.; Sato, H.; Murakami, R.; Zhang, J.; Noda, I.; Ochiai, S.; Ozaki, Y. "Comparison of Miscibility and Structure of Poly(3-Hydroxybutyrate-Co-3-Hydroxyhexanoate)/Poly(L-Lactic Acid) Blends with

Those of Poly(3-Hydroxybutyrate)/Poly(L-Lactic Acid) Blends Studied by Wide Angle X-ray Diffraction, Differential Scanning Calorimetry, and FTIR microspectroscopy", Polymer 48 (2007): 1749-1755.

Gonçalves, S. P. C.; Martins-Franchetti, S. M.; Chinaglia, D. L. "Biodegradation of the Films of PP, PHBV and Its Blend in Soil", J Polym Environ 17 (2009): 280–285.

Gu, J.D. "Microbiological Deterioration and Degradation of Synthetic Polymeric Materials: Recent Research Advances", Int Biodet Biodeg 52 (2003): 69–91.

Guadagno, L.; Naddeo, C.; Vittoria, V.; Camino, G.; Cagnani, C. "Chemical and Morphologial Modifications of Irradiated Linear Low Density Polyethylene (LLDPE)", Polym Degrad Stab 72 (2001): 175-186.

Gulmine, J.V.; Janissek, P.R.; Heise, H.M.; Akcelrud, L. "Polyethylene Characterization by FTIR", Polymer Testing 21 (2002): 557-563.

Hermida, É. B.; Yashchuk, O.; Miyazaki, S.S. "Changes in the Mechanical Properties of Compression Moulded Samples of Poly(3-Hydroxybutyrate-Co-3-Hydroxyvalerate) Degraded by Streptomyces Omiyaensis SSM 5670", Polym Degrad Stab 94 (2009): 267-271.

Kijchavengkul, T.; Auras, R.; Rubino, M.; Ngouajio, M.; Fernandez, R. T. "Development of an Automatic Laboratory-Scale Respirometric System to Measure Polymer Biodegradability", Polymer Testing 25 (2006): 1006-1016.

Krzan, A.; Hemjinda, S.; Miertus, S.; Corti, A.; Chiellini, E. "Standardization and Certification in the Area of Environmentally Degradable Plastics", Polym Degrad Stab 91 (2006): 2819-2833.

Kunioka, M.; Tamaki, A.; Doi, Y. "Crystalline and Thermal Properties of Bacterial Copolyesters: Poly(3-Hydroxybutyrate-Co-3-Hydroxyvalerate) and Poly(3-Hydroxybuyirate-Co-4-Hydroxybutyrate)", Macromolecules 22 (1989): 694-697.

Kyrikou, I.; Briassoulis, D.; Hiskakis, M.; Babou, E. "Analysis of Photo-Chemical Degradation Behaviour of Polyethylene Mulching film with Pro-Oxidants", Polym Degrad Stab 96 (2011): 2237-2252.

Luckachan, G. E.; Pillai, C. K. S. "Biodegradable Polymers- A Review on Recent Trends and Emerging Perspectives", J Polym Environ 19 (2011): 637-676.

Munaro, M.; Akcelrud, L. "Polyethylene blends: A correlation study between morphology and environmental resistance", Polym Degrad Stab 93 (2008): 43-49.

Oldak, D.; Kaczmarek, H.; Buffeteau, T.; Sourisseau, C. "Photo- and bio-degradation processes in polyethylene, cellulose and their blends studied by ATR-FTIR and Raman spectroscopies", J Materials Sci 40 (2005): 4189 – 4198.

Padermshoke, A.; Katsumoto, Y.; Sato, H.; Ekgasit, S.; Noda, I.; Ozaki, Y. "Melting behavior of poly(3-hydroxybutyrate) investigated by two-dimensional infrared correlation spectroscopy", Spectrochimica Acta Part *A* 61 (2005): 541–550.

Quental, A. C.; Hanamoto, L. S.; Felisberti, M. I. "Caracterização de Polietilenos Lineares de Baixa Densidade I. Determinação do Teor de Ramificação por Métodos Espectroscópicos", Polímeros: Ciência e Tecnologia 15 (2005): 274-280.

Rosa, D.S.; Grillo, D.; Bardi, M.A.G.; Calil, M.R.; Guedes, C.G.F.; Ramires, E.C.; Frollini, E. "Mechanical, thermal and morphological characterization of polypropylene/biodegradable polyester blends with additives", Polymer Testin*g*, vol. 28, pp. 836–842, 2009.

Roy, P.K.; Titus, S.; Surekha, P.; Tulsi, E.; Deshmukh, C.; Rajagopal, C. "Degradation of abiotically aged LDPE films containing pro-oxidant by bacterial consortium", Polym Degrad Stab 93 (2008): 1917–1922.

Santana, V. T.; Gonçalves, S. P. C.;. Agnelli, J. A. M; Martins-Franchetti, S. M. "Biodegradation of a Polylactic Acid/Polyvinyl Chloride Blend in Soil", J *Applied* Polym Sci 125 (2012): 536–540.

Sato, H.; Ando, Y.; Mitom, H.; Ozaki, Y. "Infrared Spectroscopy and X-ray Diffraction Studies of Thermal Behavior and Lamella Structures of Poly(3-hydroxybutyrate-co-3-hydroxyvalerate) (P(HB-co-HV)) with PHB-Type Crystal Structure and PHV-Type Crystal Structure", Macromolecules 44 (2011): 2829–2837.

Shah, A.; Hasan, F.; Hameed, A.; Ahmed, S. "Biological degradation of plastics: A comprehensive review", Biotechnology Advances26 (2008): 246–265.

Singh, S.; Mohanty, A. K.; Sugie, T.; Takai, Y.; Hamada, H. "Renewable resource based biocomposites from natural

fiber and polyhydroxybutyrate-co-valerate (PHBV) bioplastic", Composites: Part A 39 (2008): 875–886.

Solaro, R.; Corti, A.; Chiellini, E. "A New Respirometric Test Simulating Soil Burial Conditions for the Evaluation of Polymer Biodegradation", J Polym Environment 6 (1998): 203-208.

Sudhakar, M.; Doble, M.; Murthy, P. S.; Venkatesan, R. "Marine microbe-mediated biodegradation of low- and high-density polyethylenes", Int Biodet Biodeg 61 (2008): 203–213.

Suresh, B.; Maruthamuthu, S.; Khare, A.; Palanisamy, N.; Muralidharan, V. S.; Ragunathan, R.; Kannan, M.; Pandiyaraj, K. N. "Influence of thermal oxidation on surface and thermo-mechanical properties of polyethylene", J Polym Res 18 (2011): 2175–2184.

Starka, N. M.; Matuana, L. M. "Surface chemistry changes of weathered HDPE/wood-flour composites studied by XPS and FTIR spectroscopy", Polym Degrad Stab 86 (2004): 1–9.

Vilaplana, F.; Strömberg, E.; Karlsson, S. "Environmental and resource aspects of sustainable biocomposites", *Polym Degrad Stab* 95 (2010): 2147-2161.

Volke-Sepulveda, T.; Saucedo-Castaneda, G.; Gutierrez-Rojas, M.; Manzur, A.; Favela-Torres, E. "Thermally Treated Low Density Polyethylene Biodegradation By Penicillium pinophilum and Aspergillus niger", J Applied Polym Sci 83 (2002): 305–314.

Weng, Y.X.; Wang, X.L.; Wang, Y. Z. "Biodegradation behavior of PHAs with different chemical structures under controlled composting conditions", Polymer Testing 30 (2011): 372–380.

Yoshie, N.; Saito, M.; Inoue, Y. "Structural transition of lamella crystals in a isomorphous colopymer, Poly(3-hydroxybutyrate-co-3-hydroxyvalerate)", Macromolecules 34 (2001): 8953-8960.

Analysis of the Damping of Sandwich Materials and Effect of the Characteristics of the Constituents

Mustapha Assarar[1]*, Abderrahim El Mahi[2], Jean-Marie Berthelot[3]

[1]University of Reims Champagne-Ardenne, LISM EA 4695, IUT de Troyes, 9 rue de Québec 10026 Troyes, France
[2]University of Maine, LAUM, UMR CNRS N°6613, avenue Olivier Messiaen, 72085 Le Mans cedex 9, France
[3]ISMANS, Institute for Advanced Materials and Mechanics, 44 avenue Bartholdi, 72000 Le Mans, France

*[1]mustapha.assarar@univ-reims.fr; [2]abderrahim.elmahi@univ-lemans.fr; [3]jmberthelot@ismans.fr

Abstract

The purpose of the paper is to analyse the damping of sandwich composites made of foam core and laminated skins. Damping parameters are investigated in the case of the bending vibrations of clamped-free beams. Modelling of the damping of the sandwich materials is established using a finite element analysis formulated on the sandwich material theory. Damping modelling is based on the evaluation of the different energies dissipated in the material directions of the core and the layers of the skins. The results obtained in the case of the bending vibrations of beams show a good agreement with the experimental results derived from an experimental investigation. Next, a parametric study is implemented to identify the effect of the characteristics of the constituents on the damping of the sandwich composites.

Keywords

Sandwich Materials; Damping; Finite Element Analysis; Vibration Testing

Introduction

Sandwich composite materials are increasingly being used in a variety of industrial applications such as, marine, aerospace, automobile industry etc. The use of sandwich construction is the result of an increasing demand for light and strong structures. Weight saving is a dominant factor in the transport sectors such as high speed trains, high speed boats, cars etc. The sandwich concept takes advantages over single skin laminated structures in terms of flexural properties with a reduced weight. Flexural stiffness and strength are just two of a variety of design criteria to be considered.

The problem to dissipate energy in structures is an important consideration in mechanical design of structures. Sufficient damping is needed to reduce damping of structures, further to avoid fatigue fracture. Generally, the damping of metal structures is low. For fibre reinforced materials, the damping is higher and depends on the constituent properties. In the vibrations of structures made of sandwich materials, the damping depends on the constituent properties and a high part of the energy is dissipated by the transverse shear effects induced in the sandwich core, which leads to increase the damping of materials.

General considerations on the damping of composite materials are developed in the review of Chandra et al (Chandra, Singh, Gupta, 1999). Firstly, the review considers the different damping processes induced in fibre reinforced composites, resulting from the viscoelastic behaviour of the matrix, the damping of the fibre-matrix interphase, the damping due to damage and the thermo-elastic damping. Next, models for prediction of damping are analysed: the correspondence principle which leads to the introduction of the complex moduli, the stored energy approach, the macro-mechanical description states that the energy dissipated can be considered as the superposition of the energies dissipated in longitudinal, transverse and shear behaviour. At last, the review considers the application of damping models to obtain high damping of laminates combining interleaving viscoelastic layers and fibre arrangement in the different layers of the laminates. Other works on the vibrations of sandwich materials have been reported in the survey papers of Nakra (Nakra, 1981 & 1984). Based on these works, great contributions (Vaswani, Asnani, Nakra, 1988 & Moser, Lumassegger, 1988 & He, Rao, 1992 & Rikards, 1993) were made to the introduction of the concept of a complex modulus, using the elastic-viscoelastic correspondence principle. In this concept, the real part

of the complex modulus represents the elastic stiffness and the imaginary part is associated with the energy dissipation. More recently, the concept of complex modulus was associated with a high-order shear deformation theory by Meunier and Shenoi (Meunier, Shenoi, 2001) to model the damping of sandwich plates. Extensive analyses of the damping of rectangular laminate plates were developed by Berthelot and Sefrani (Berthelot, Sefrani, 2004 & Berthelot, 2006) using the Ritz method that was then extended (Berthelot, 2006 & Berthelot, Sefrani, 2006) to the case of laminates with interleaved viscoelastic layers. The Ritz method is restricted to the analysis of rectangular plates. In the case of complex shape structures, it is necessary to consider a finite element analysis (El Mahi, Assarar, Sefrani, Berthelot, 2008). A finite element was developed by Araújo et al. (Araújo, Mota Soares, Mota Soares, 2010) for the analysis of active sandwich plates with a viscoelastic core and laminated anisotropic face layers, as well as piezoelectric sensor and actuator layers. The elastic layers were modelled with a first order shear deformation theory, and viscoelastic core with a three order shear deformation theory. The dynamic problem is solved in the frequency domain with frequency dependent material properties for the core. Identification of the frequency dependent properties of viscoelastic core materials was considered in (Araújo, Mota Soares, Mota Soares, Herskovits, 2010). Modelling of the damping of sandwich materials has been investigated by Assarar et al. in (Assarar, El Mahi, Berthelot, 2009) using a finite element analysis, and the results derived from which are then applied to the experimental evaluation of the damping parameters of the sandwich materials.

The purpose of the present paper is to consider the modelling of damping of sandwich materials using a finite element analysis based on the sandwich material theory. The results derived from this analysis are then applied to the experimental evaluation of the damping parameters of sandwich materials in the case of the flexural vibrations of beam specimens. At last a parametric study is implemented to identify the influence of the characteristics of the constituents on the damping of sandwich structures.

Modelling the Damping of Sandwich Composite Materials and Structures

To describe the flexural behaviour of sandwich material test specimens, laminate theory or sandwich material theory (Berthelot, 1999 & 2012) can be used,

which leads to similar results.

Therefore, the vibrations of the test specimens are investigated in the paper using the QUAD4S finite element type of PERMAS software. This finite element analysis uses the classical sandwich material theory for which the in-plane displacements of the core are linear functions of the z coordinate through the foam core thickness h_c as well the in-plane displacements are uniform through the thicknesses h_s of the skins of the sandwich composite. Moreover, the transverse displacement w is considered as independent of the z coordinate. Thus, the strain ε_{zz} is neglected in the foam core and in the skins.

The finite element analysis gives (Fig. 1) the values of the in-plane stresses σ_{xx}, σ_{yy}, σ_{xy}, in each layer k of the skins of each finite element e of the structure under consideration:

$$\sigma_{xxk}, \ \sigma_{yyk}, \ \sigma_{xyk}, \tag{1}$$

and the values of the stresses σ_{xx}, σ_{yy}, σ_{xy}, σ_{xz}, σ_{yz}, on the lower face (l) and the upper face (u) of core of each finite element e of the structure (Fig. 1):

$$\sigma_{xx\mathrm{lc}}, \ \sigma_{yy\mathrm{lc}}, \ \sigma_{xy\mathrm{lc}}, \ \sigma_{xz\mathrm{lc}}, \ \sigma_{yz\mathrm{lc}},$$
$$\sigma_{xx\mathrm{uc}}, \ \sigma_{yy\mathrm{uc}}, \ \sigma_{xy\mathrm{uc}}, \ \sigma_{xz\mathrm{uc}}, \ \sigma_{yz\mathrm{uc}}, \tag{2}$$

with

$$\sigma_{xz\mathrm{uc}} = \sigma_{xz\mathrm{lc}} = \sigma_{xzc}, \qquad \sigma_{xz\mathrm{uc}} = \sigma_{yz\mathrm{lc}} = \sigma_{yzc}. \tag{3}$$

Next, the evaluation of the damping is derived from the energy method to perform the evaluation of the different energies evaluated in the material directions as follows.

- In-Plane Strain Energy

The in-plane energy U_d^e stored in a given finite element e can be expressed as a function of the in-plane strain energies related to the material directions as:

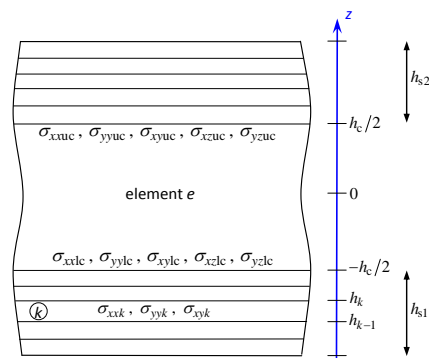$$U_\mathrm{d}^e = U_1^e + U_2^e + U_6^e, \tag{4}$$

FIG. 1 STRESSES DERIVED FROM FINITE ELEMENT ANALYSIS IN THE LAYERS OF THE SKINS AND IN THE CORE

with

$$U_1^e = \frac{1}{2} \iiint_e \sigma_1\, \varepsilon_1 \ \mathrm{d}x\,\mathrm{d}y\,\mathrm{d}z,$$

$$U_2^e = \frac{1}{2} \iiint_e \sigma_2\, \varepsilon_2 \ \mathrm{d}x\,\mathrm{d}y\,\mathrm{d}z, \qquad (5)$$

$$U_6^e = \frac{1}{2} \iiint_e \sigma_6\, \varepsilon_6 \ \mathrm{d}x\,\mathrm{d}y\,\mathrm{d}z,$$

where the integrations are extended over the volume of the finite element e. ε_1, ε_2, ε_6 and σ_1, σ_2, σ_6 are respectively the in-plane strains and stresses related to the material directions of the layer k of the skins or the core of sandwich material.

- Transverse Shear Strain Energy

The transverse shear energy for a given finite element e can be expressed in the material directions as:

$$U_\mathrm{d}^e = U_{44}^e + U_{55}^e, \qquad (6)$$

with

$$U_{44}^e = \frac{1}{2} \iiint_e \sigma_4\, \gamma_4 \ \mathrm{d}x\,\mathrm{d}y\,\mathrm{d}z,$$
$$\qquad\qquad\qquad\qquad (7)$$
$$U_{55}^e = \frac{1}{2} \iiint_e \sigma_5\, \gamma_5 \ \mathrm{d}x\,\mathrm{d}y\,\mathrm{d}z,$$

where the integrations are extended over the volume of the finite element e. σ_4 and γ_4 are respectively the transverse shear stress and strain in plane (T, T') of material in the layer k of the skins or in the core of sandwich material. σ_5 and γ_5 are the transverse shear stress and strain in plane (L, T'') of the element.

Finally, the damping of the finite element assemblage can be evaluated by extending the energy formulation approach considered in (Berthelot, 2006). The total strain energy stored in the laminated structure is given by:

$$U_\mathrm{d} = U_{11} + U_{22} + 2U_{12} + U_{66} + U_{44} + U_{55}, \qquad (8)$$

with

$$U_{ij} = \sum_{\text{elements}} U_{ij}, \qquad (9)$$

Where U_{ij} the strain energies stored in the finite element assemblage is obtained by summation on the element.

The energy dissipated by damping in the layer k of the skins or in the core of the sandwich material of the element e is derived from the strain energy stored in the layer or in the core as:

$$\Delta U_l^e = \psi_{11l}^e U_{11l}^e + \psi_{22l}^e U_{22l}^e + 2\psi_{12l}^e U_{12l}^e + \psi_{66l}^e U_{66l}^e$$
$$+\ \psi_{44l}^e U_{44l}^e + \psi_{55l}^e U_{55l}^e \qquad (10)$$

These coefficients are related to the material directions (L, T, T') of the layer k of the skins $(l = k)$ or of the core $(l = \mathrm{c})$: ψ_{11l}^e and ψ_{22l}^e are the damping coefficients in traction-compression in the L direction and T direction of the foam, respectively; ψ_{12l}^e is the in-plane coupling coefficient; ψ_{66l}^e is the in-plane shear coefficient; ψ_{44l}^e and ψ_{55l}^e are the transverse shear damping coefficients in planes (T, T') and (L, T'), respectively.

The damping energy dissipated in the element e is next obtained by summation on the core and on the layers of the skins of element e as:

$$\Delta U = \Delta U_\mathrm{c}^e + \sum_{k=1}^{n} \Delta U_k^e. \qquad (11)$$

Finally, the damping of the finite element assemblage is characterised with the damping coefficient ψ of the assemblage derived from relation:

$$\psi = \frac{\Delta U}{U_\mathrm{d}}. \qquad (12)$$

The in-plane strain energies U_{11}, U_{22}, $2U_{12}$, U_{66} and the transverse shear strain energies U_{44}, U_{55} related to the material directions, can be expressed as functions of both the in-plane stresses σ_{xx}, σ_{yy}, σ_{xy} and the transverse shear stresses σ_{yz}, σ_{xzy} related to the finite element directions (x, y, z). The formulation of the energies expressed in Eq. (5) and (7) as function of mechanical characteristics of constituents (skins and core) and stresses given by Expression (2) was detailed in the modelling of damping developed Berthelot et al.in (Berthelot, Assarar, Sefrani, El Mahi 2008) and by Assarar et al. in (Assarar, El Mahi, Berthelot, 2009). The approach described in this section as well as the modelling of the damping developed in (Berthelot, Assarar, Sefrani, El Mahi 2008 & Assarar, El Mahi, Berthelot, 2009) allow identifying the effect of characteristics of the constituents particularly the influence of skins on the damping of sandwich structures.

Experimental Procedure

Determination of the Dynamic Properties of the Test Specimens

The damping characteristics of the materials were obtained by subjecting beams to flexural vibrations.

The equipment used is shown in Fig. 2. The test specimen is supported horizontally as a cantilever beam in a clamping block. An impulse hammer, model PCB086 B03, is used to induce the excitation of the flexural vibrations of the beam. A force transducer positioned on the hammer allows us to obtain the excitation signal as a function of the time. The width of the impulse and thus the frequency domain is controlled by the stiffness of the head of the hammer. The beam response is detected by using a laser vibrometer Polytec (OFV 302 R optical head and OFV 3000 conditioner) which measures the velocity of the transverse displacement. Then, the excitation and the response signals are digitalized and processed by a dynamic analyzer of signals developed by Siglab Company. This analyzer associated with a PC computer performs the acquisition of the signals, controls the acquisition conditions (sensibility, frequency range, trigger conditions, etc.), and further operates the analysis of the signals acquired (Fourier transform, frequency response, mode shapes, etc.). In addition, the signals and the associated processings can be saved for post-processing. The system allows the simultaneous acquisition of two signals with a maximum sampling frequency of 50 kHz with a resolution of 13 bits for each channel. The analytical bending response of a clamped-free beam submitted to a concentrated loading has been established in paper (Berthelot, Sefrani, 2004). This analytical response can be applied using the viscous damping modelling or the complex stiffness modelling. Thus, the process of the determination of the dynamic parameters of the test specimens was implemented by fitting the experimental responses with the analytical bending response. The curve fitting was obtained by a least square method by means of the optimisation toolbox of Matlab. The experimental and analytical curve fitting allows us to derive the values of the natural frequencies f_i, and the modal damping coefficient ξ_i (case of damping using viscous damping modelling) or the loss factor η_i (case of damping using the complex stiffness model), related to the specific damping capacity by the relation $\psi_i = 2\pi\eta_i$. The specific damping capacity is usually used to characterise the ratio of the energy dissipated to the energy stored in a structure or an element of structure.

Materials

Sandwich materials were constructed with glass fibre laminates as skins and with PVC closed-cell foams as core. The glass fibre laminates of the skins are cross-ply laminates composed of unidirectional layers of E-glass fibres in an epoxy matrix, arranged in the sequence [0°/90°/90°/0°]. The unidirectional layers were fabricated with unidirectional fabrics of weight 300 gm^{-2} with glass fibres aligned in a single direction.
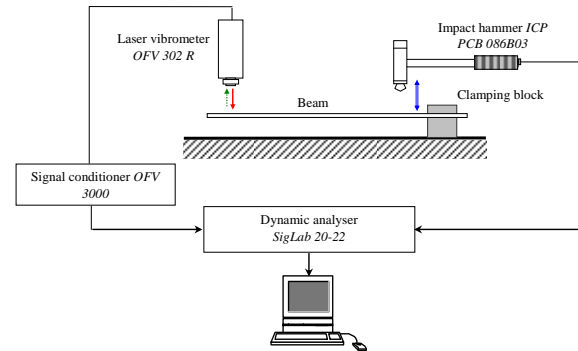

FIG. 2 EXPERIMENTAL EQUIPMENT FOR THE ANALYSIS OF BEAM VIBRATIONS

The engineering constants of the unidirectional layers referred to the material directions (L, T, T') or (1, 2, 3) were measured in static tests as mean values of 10 tests for each constant. The values obtained are reported in Table 1. The experimental damping analysis of the laminates has been investigated in (Berthelot, Sefrani, 2006 & Berthelot, Assarar, Sefrani, El Mahi, 2008) and the values of the loss factors derived from this analysis are reported in Fig. 2a. The PVC closed-cell foams were supplied in panels with thickness of 15 mm, and two foams considered differing in their densities: 60 kg m^{-3} and 200 kg m^{-3}. Mechanical characteristics of the foams were measured in static tensile tests for the Young's modulus and the Poisson's ratio, and in static shear tests for the shear modulus. The results obtained show that the foams are isotropic and the modulus values derived are reported in Table 2. The dynamics properties of the core foam are deduced from the experimental investigation and modelling analysis according to the procedure described in (Assarar, El Mahi, Berthelot, 2012). The values of the dynamics properties deduced from this analysis are reported in Figures 2b and 2c.

Sandwich materials were constructed both with these foams and cross-ply glass-fibre laminates prepared by hand lay-up process, which leads to a nominal thickness of 1.2 mm for the sandwich skins.

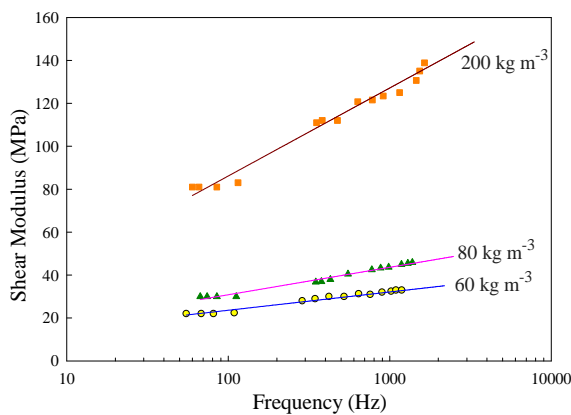TABLE 1. ENGINEERING CONSTANTS OF THE UNIDIRECTIONAL GLASS FIBRE LAYERS.

E_L (GPa)	E_T (GPa)	G_{LT} (GPa)	v_{LT}
29.9	7.5	22.5	0.24

TABLE 2. CHARACTERISTICS OF PVC FOAMS DERIVED FROM STATIC TESTS

Density of the foam (kg m^{-3})	Young's modulus (MPa)	Poisson's ratio	Shear modulus (MPa)
60	59	0.42	22
200	240	0.45	80
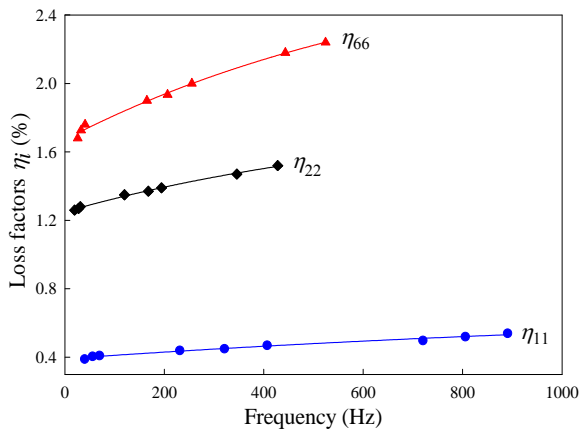
(a)

(b)
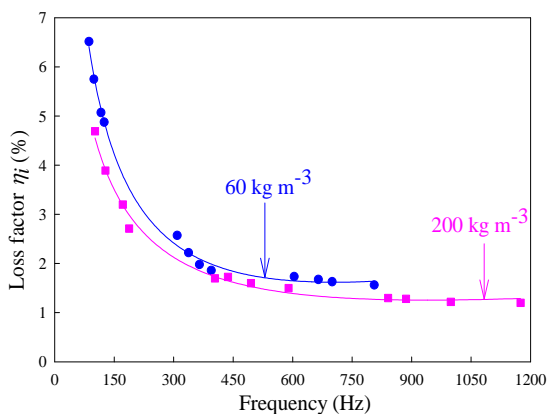
(c)

FIG. 3 DYNAMICS PARAMETERS OF THE CONSTITUENTS OF THE SANDWICH MATERIALS AS A FUNCTION OF FREQUENCY: (a) LOSS FACTORS IN THE MATERIAL DIRECTIONS OF THE UNIDIRECTIONAL GLASS FIBRE LAYERS, (b) SHEAR MODULUS OF FOAMS (c) DAMPING OF FOAMS DEDUCED FROM EXPERIMENTAL INVESTIGATION AND FINITE ELEMENT ANALYSIS.

Characteristics Factors of the Damping of THE Sandwich Materials

Analysis of the Damping of Sandwich Materials

Investigation of the damping has been implemented in the case of sandwich materials considered in previous Subsection B. The experimental investigation was carried out in the case of the flexural vibrations of clamped-free beams. An aluminium spacer was added in the root section which was closely clamped in a rigid fixture. The free length of the beams was equal to 250, 300, 350 and 400 mm, and the beam width was equal to 40 mm.

The experimental results obtained have been compared with the results deduced from the modelling considered in Section II. This analysis takes into account the variation of the damping of the unidirectional layers of the skins (Fig. 3a), as well as the variation of the shear modulus and damping of foam core as functions of the frequency (Fig. 3b and 3c).

Comparison has been made in Fig. 4 between the results deduced from the experimental investigation and from modelling for the sandwich materials, in the case of core with foams of 60 and 200 kg m^{-3}, showing a good agreement between the experimental results and the results deduced from modelling. Furthermore, it is observed that damping as a function of the frequency is discontinuous from one mode to the other, due to a change of the distribution of the strain energies according to the mode. Indeed, the evolution of the damping of the sandwich materials depends on different factors as demonstrated in (Assarar, El Mahi, Berthelot, 2009).

Energies Dissipated in the Core and Skins

Fig. 5 reports the energies dissipated in the core and in the skins for the first four modes of the bending vibrations of the sandwich beams of lengths 250, 300, 350 and 400 mm, in the case of foam cores of density 60 and 200 kg m^{-3}, respectively. These results are derived from a finite element analysis. For the densities of the foam core equal to 60 kg m^{-3}, the energy dissipated in the foam core is clearly higher than that in the skins. Likewise, it is observed an increase of the energy dissipated in the foam core and a decrease of the energy dissipated in the skins when the frequency as well as the mode number increases which can be attributed to the dominant effect of the transverse shear in the foam core, resulting from the low values of the shear modulus of the foam core and

the increment with the mode because of the mode shape. In contrast, for the density of 200 kg m⁻³ of the foam core, the energy dissipated in the foam core increases with the frequency and the mode number, when the energy dissipated in the skins decreases. Moreover, the energy dissipated in the foam core is smaller for the modes 1 and 2 and higher for the mode 4. For this foam density the value of the shear modulus is high, and the results observed can be associated with two different elements: the distribution of the energy in the core and skins according to the modes, and the increase of the shear modulus as a function of the frequency. For the modes 1 and 2, the transverse deformation of the foam core is less pronounced than that for the mode 4, which yields, with a high value of the shear modulus of the foam core, a low energy dissipated in the foam core.

The preceding effect according to the mode shape is also underlined when the evolution of the energies dissipated is taken into consideration as a function of the ratio of the core thickness to the skin thickness (Fig. 6). In this figure, the dissipated energies derived from finite element analysis are reported for the first three modes of the bending vibrations of sandwich beams of 350 mm length and a foam density of 60 kg m⁻³. Skins of the beams are [0°/90°/90°/0°] cross-ply laminates. It is observed that the energy dissipated in the core increases with the thickness of the foam core. For the first mode, the energy dissipated in the skins is higher than that in the foam core for low values of core thickness: values of core thickness smaller about four times than the skin thicknesses. Additionally, the energy dissipated in the foam core increases when the mode number rises, which shows clearly that the part of the transverse shear energy dissipated in the foam core increases with the mode number. This effect is induced by the shapes of the vibration mode.
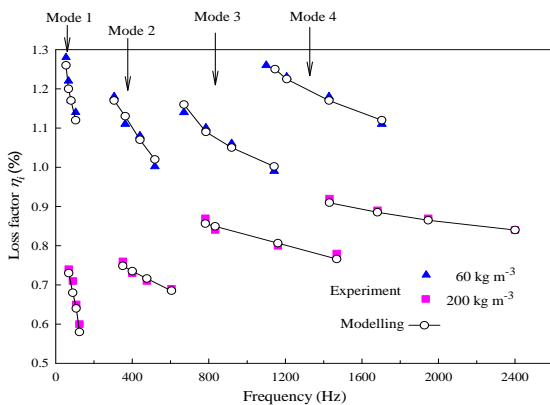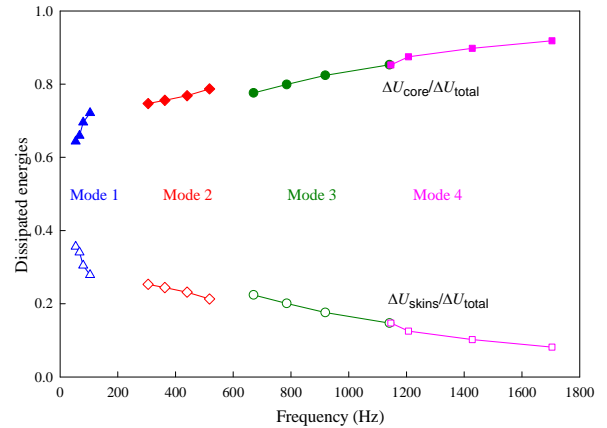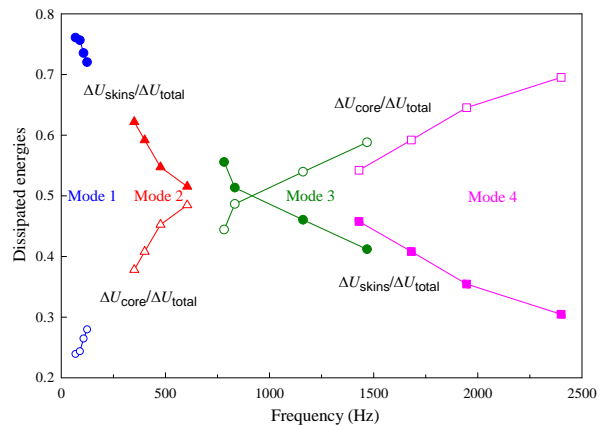

FIG. 4 COMPARISON BETWEEN THE RESULTS DEDUCED FROM EXPERIMENT AND MODELLING FOR THE DAMPING OF SANDWICH MATERIALS, IN THE CASE OF CORE WITH FOAMS OF DENSITY 60 AND 200 kg m⁻³

(a)

(b)

FIG. 5 ENERGIES DISSIPATED IN THE CORE AND IN THE SKINS FOR THE FIRST FOUR MODES OF THE BENDING VIBRATIONS OF THE SANDWICH BEAMS OF LENGTHS 250, 300, 350 AND 400 MM : (a) IN THE CASE OF A FOAM CORE OF DENSITY 60 KG M–3, (b) IN THE CASE OF A FOAM CORE OF DENSITY 200 KG M–3
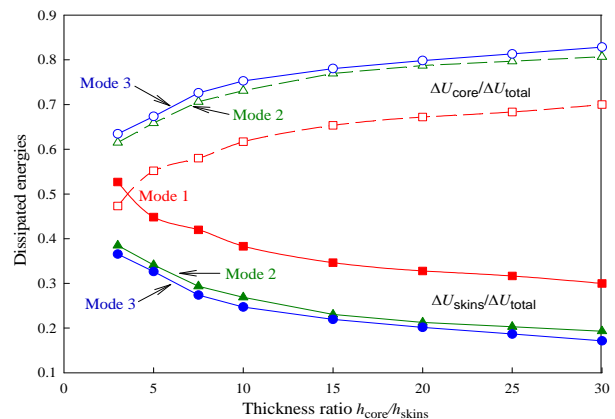

FIG. 6 ENERGIES DISSIPATED IN THE CORE AND IN THE SKINS FOR THE FIRST THIRD MODES OF THE BENDING VIBRATIONS OF SANDWICH BEAMS OF LENGTHS 350 MM AS FUNCTIONS OF THE RATIO OF CORE AND SKINS THICKNESSES, IN THE CASE OF A FOAM CORE OF DENSITY 60 KG M–3 AND [0°/90°/90°/0°] SKINS.

Influence of the Shear Modulus of the Foam Core

For a given damping of the foam core, one of the principal factors which govern the damping of

sandwich materials is the shear modulus of the foam core. Fig. 7 shows the results derived from a finite element analysis for the damping of sandwich materials as a function of the value of the shear modulus of the foam core, in the case of the first two modes of sandwich beams with lengths 250, 300, 350 and 340 mm. The results show clearly that an increase of the shear modulus of the foam core yields a significant decrease of the damping of sandwich materials: when the shear modulus is multiplied by 8, the sandwich damping is divided by a factor about 4 for the first mode and about 3 for the second mode. For a given mode and shear modulus of the foam core, damping of sandwich materials decreases when the frequency increases, then when the length of the sandwich beams is increased. This result can be associated with a decrease in the part of the transverse shear strain energy stored in the foam core. The variation of the damping from one mode to the other is associated with the distribution of the strain energies in the skins and the core. Elements on this aspect are considered in the following subsections.
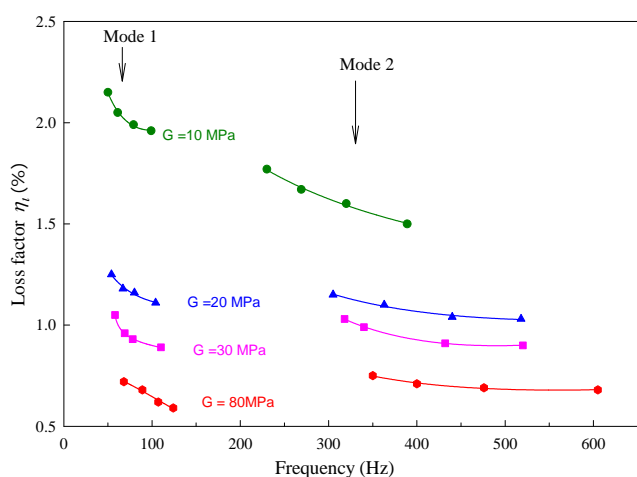
FIG. 7 INFLUENCE OF THE SHEAR MODULUS OF THE FOAM CORE ON THE DAMPING OF SANDWICH MATERIALS, FOR THE FIRST TWO MODES OF SANDWICH BEAMS.

Effect of the Core Thickness on the Damping of Sandwich Materials

Fig. 8 shows the evolution of the damping of the sandwich materials as a function of the thickness of the foam core, for a foam density of 60 kg m^{-3}. Two different evolutions of the loss factors are observed a function of the frequency according to the foam thickness: for thicknesses of the foam core of 3.5, 5 and 7.5 mm, the loss factor increases as a function of the frequency (Fig. 8a), when the loss factor decreases for thicknesses of the core higher or equal to 10 mm (Fig. 8b). These two different behaviours can be associated

with the evolution of the distribution of the energies dissipated in the core and skins as a function of the core thickness. For low values of the core thickness, the effect of the damping of the skins is dominant and the increase of the damping of the skin layers with frequency (Fig. 3a) induces an increase of the resultant damping of the sandwich materials. For high values of the skin thicknesses, the effect of the damping of foam core is dominant and the increase of the shear modulus of the foam with the frequency (Fig. 3b) as well as the decrease of the foam damping (Fig. 3c) lead to a decline of the damping of the sandwich materials as a function of the frequency.
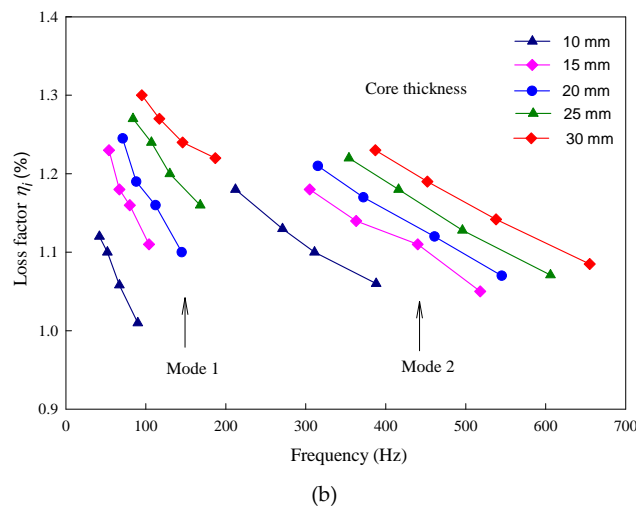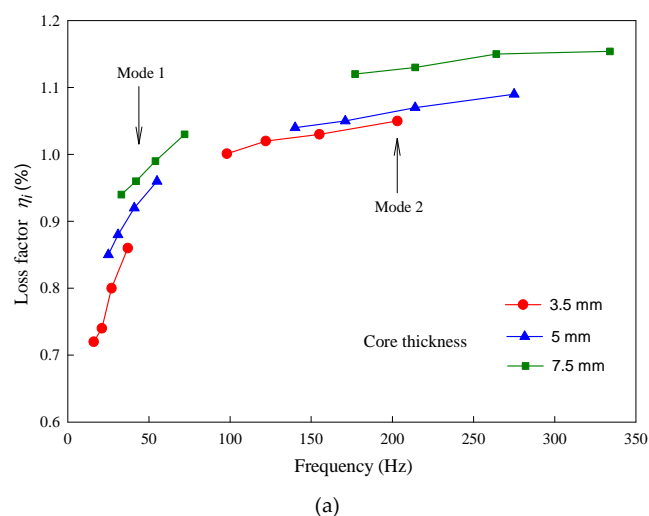

(a)

(b)

FIG. 8 EVALUATION OF THE DAMPING OF THE SANDWICH MATERIALS FOR VARIOUS THICKNESSES OF THE FOAM CORE, IN THE CASE OF [0°/90°/90°/0°] CROSS-PLY LAMINATE SKINS AND A FOAM DENSITY OF 60 KG M-3: (a) THICKNESS CORE SMALLER THAN 7.5 MM AND (b) THICKNESS CORE HIGHER THAN 10 MM.

Effect of the Skin Thickness on the Damping of Sandwich Materials

Fig. 9a shows the evolution of the damping of the

sandwich materials as a function of the thickness of the foam core, for a foam density of 60 kg m^{-3}, in the case of the first two bending modes of sandwich beams with lengths 250, 300, 350 and 400 mm. It is observed that the loss factor decreases as a function of the frequency for each thickness of skins, which results from the evolution of the distribution of the energies dissipated in the core and skins (Fig. 5 and 6). Indeed, the effect of the damping of foam core is dominant as well as the decrease of the foam damping (Fig. 3c), which leads to a decrease of the damping of the sandwich materials as a function of the frequency. Fig. 9b gives the evolution of damping according to the ratio of the skin thicknesses to the core thickness. The damping rises when the ratio of the thicknesses increases with a maximum at about 7.5 which corresponds to a thickness of 2 mm skins. In fact, when the thickness of the skin varies from 1 to 2 mm, the flexural stiffness of skins increases and imposes an important transverse shear stress on the core and consequently an increase of the energies dissipated, leading to an increment of the damping of the sandwich material. When the thickness of skins is higher than 2 mm, flexural stiffness increases but the effect of the thickness of skins on the damping becomes significant. In this case, damping of sandwich materials is dominated by the damping of the skins.

Effect of the Type of Skin on the Damping of Sandwich Materials

Two materials sandwiches composed of skins with various reinforcements and core foam with density of 60 kg m-3 and 15mm thickness have been considered. The first one is a sandwich materials with [0°/90°/90°/0°]s cross-ply laminates and the second one is a sandwich materials with serge laminate. Fig. 10 compares the results obtained in the case of both sandwich materials, for the first two bending modes. The results show that the damping of serge sandwich is clearly higher than that of cross-ply laminates sandwich. In addition to the dominant effect of the core foam on the damping of the sandwich materials, these results show the effect of the reinforcement type of the skins on the damping of the sandwich materials.

Effect of the Skins Orientations on the Damping of Sandwich Materials

Sandwich materials made of unidirectional fibre skins of 2 mm thickness and foams core of density 60 kg m^{-3} and 15 mm thick have been in consideration together with various orientations of skins fibres: 0°, 15°, 30°,

45°, 60°, 75° and 90°. Fig. 11a shows the evolution of the damping according to the frequency for the first two bending modes of beams and for different skins orientations. For a given orientation of the fibres, it is observed that damping decreases when the frequency is increased. Skins orientations slightly influence the global damping of sandwich materials in the bending modes. The variations of the damping with fibre orientations for the first two modes are given in Fig. 11b. The results show that damping is maximum for fibre orientation of about 0° for the first mode, when a maximum of about 45° is observed in the case of the second mode, which is attributed to the distribution of the energies dissipated in the skins and the core of the sandwich materials.
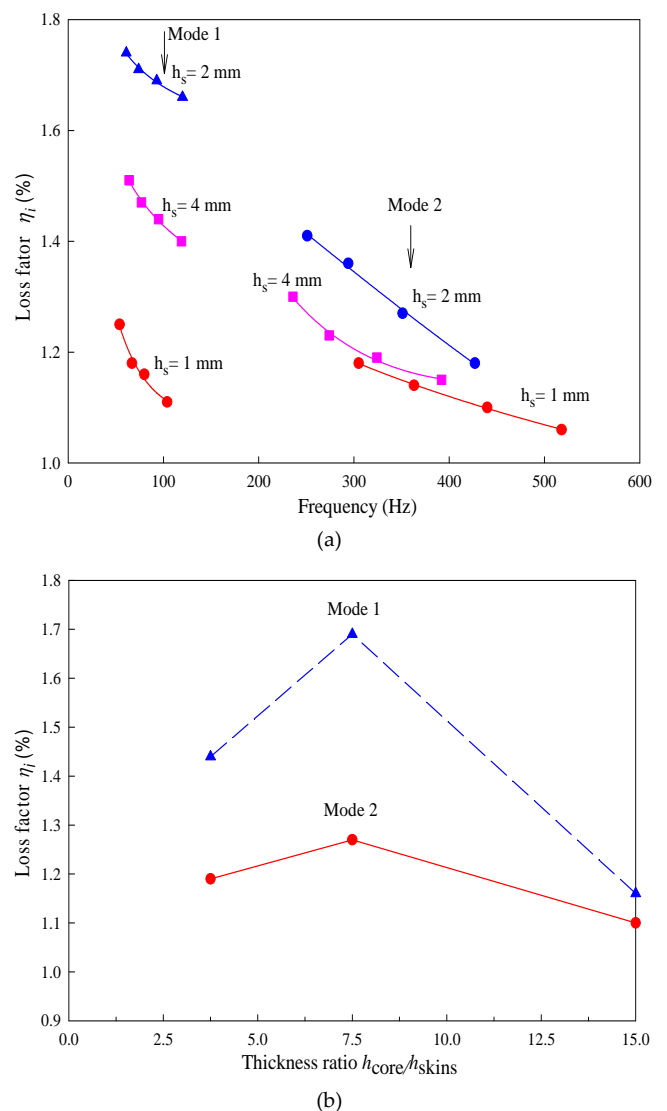

(a)

(b)

FIG. 9 EVALUATION OF THE DAMPING OF THE SANDWICH MATERIALS FOR VARIOUS THICKNESSES OF THE SKIN, IN THE CASE OF (0I/90I)S CROSS-PLY LAMINATE SKINS AND A FOAM DENSITY OF 6060 KG M-3: (a) AS FUNCTION OF SKINS THICKNESSES VALUES, (b) AS FUNCTIONS OF THE RATIO OF CORE AND SKINS THICKNESSES
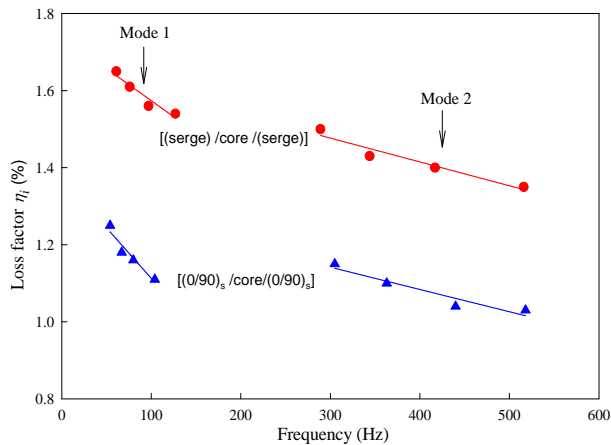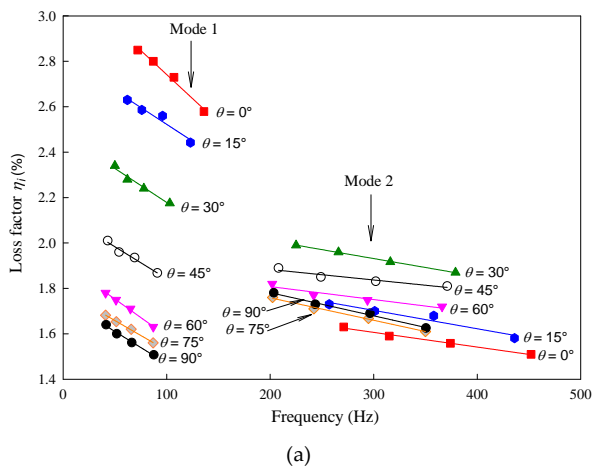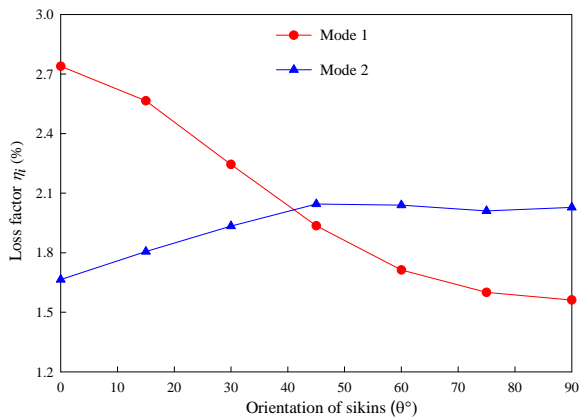
FIG. 10 INFLUENCE OF THE REINFORCEMENT TYPE OF THE SKINS ON THE DAMPING OF SANDWICH MATERIAL, FOR THE FIRST TWO MODES OF BEAMS, IN THE CASE OF CORE WITH FOAM OF 60 KG M-3.


(a)

(b)

FIG. 11 EVALUATION OF THE DAMPING OF THE SANDWICH MATERIALS FOR DIFFERENT SKINS ORIENTATIONS, IN THE CASE OF UNIDIRECTIONAL LAMINATE AND WITH FOAM CORE OF 60 KG M-3: (A) AS A FUNCTION OF THE FREQUENCY, (b)) AS FUNCTIONS OF SKINS ORIENTATIONS.

The relative variations of the energy dissipated in skins and core are reported in Fig. 12. It is observed in the case of the first mode that the energy dissipated in skins increases according to the orientation of skins fibres, while the energy dissipated in the foam core

decreases due to the decline of the shear strain in the foam. In fact, when skins fibres are disoriented, the flexural stiffness of the skins decreases, which reduces the stress imposed by skins on the core. This process induces a decrease of the shear energy of the core foam. In the second mode, the variations of the energies dissipated in skins and foam core are similar to those observed in the first mode with a light difference for an orientation of skins fibres of 40°. In this orientation appears the coupling between bending and twisting.
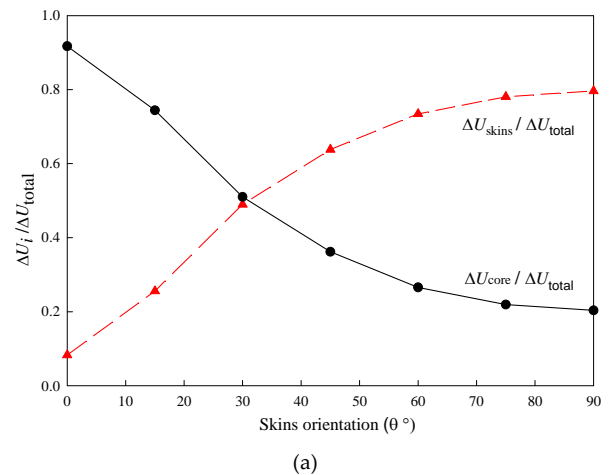
(a)
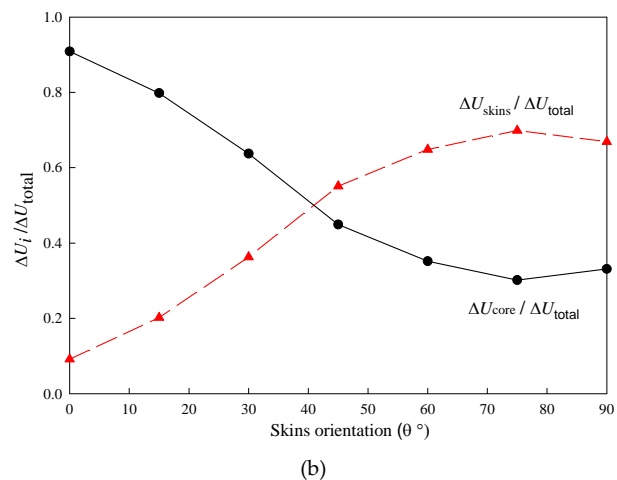
(b)

FIG. 12 ENERGIES DISSIPATED IN THE CORE AND IN THE SKINS FOR DIFFERENT SKINS ORIENTATIONS, IN THE CASE OF SANDWICH BEAMS OF LENGTHS 350 MM AS FUNCTIONS OF THE ORIENTATION SKINS, (a) FIRST MODE, (b) SECOND MODE.

Conclusions

Modelling of the damping properties of sandwich materials was implemented considering the theory of sandwich plates and using a finite element analysis. The analysis derives the strain energies stored in the material directions of the foam core and in the material directions of the layers of the skins. Further, the energy dissipated by damping in the structure can

be obtained as a function of the strain energies and the damping coefficients associated to the different energies stored in the material directions of the core and the layers of the skins. Next, a parametric study is performed to identify the influence of the characteristics of the constituents on the damping of the sandwich materials. These results obtained show that the main factors influencing the damping of the sandwich materials are: the natural frequencies, the shear modulus of foam, the thickness of the foam, the distribution of the energies stored in the foam and in the skins, the type of reinforcement and the thickness of skins.

REFERENCES

Araújo, A.L., Mota Soares, C.M., Mota Soares, C.A. (2010). A Viscoelastic Sandwich Finite Element Model for the Analysis of Passive, Active and Hybrid Structures. Applied Composite Materials 17: 529–542.

Araújo, A.L., Mota Soares, C.M., Mota Soares, C.A., Herskovits J. (2010). Characterisation by Inverse Techniques of Elastic, Viscoelastic and piezoelectric Properties of Anisotropic Sandwich Adaptive Structures, Applied Composite Materials 17 (5) 543–556.

Assarar, M., El Mahi, A., Berthelot, J.-M. (2012) "Evaluation of the Dynamic Properties of PVC Foams under Flexural Vibrations" Composite Structures, Vol 94, 1919–1931.

Assarar, M., El Mahi, A., Berthelot, J.-M. (2009). Damping Analysis of Sandwich Composite Materials, Journal of Composite Materials, 43(13):1461-1485.

Berthelot, J-M. (2012). Matériaux Composites. Comportement Mécanique et Analyse des Structures. Tec & Doc, Paris, 5th edition.

Berthelot, J-M, Assarar, M, Sefrani, Y, El Mahi, A. (2008). Damping Analysis of Composite Materials and Structures Composites Structures. Vol 82, pp. 189-204

Berthelot, J-M. (2006). Damping Analysis of Orthotropic Composites with Interleaved Viscoelastic Layers: Modeling. Journal of Composite Materials. 40:1889-1909.

Berthelot, J-M, Sefrani, Y. (2006). Damping Analysis of Orthotropic Composites with Interleaved Viscoelastic Layers: Experimental Investigation and Discussion. Journal of Composite Materials. 40:1911-1931.

Berthelot, J-M. (2006). Damping Analysis of Laminated Beams and Plates Using the Ritz Method. Composite Structures. 74:186-201.

Berthelot, J-M, Sefrani, Y. (2004). Damping Analysis of Unidirectional Glass and Kevlar Fibre Composites. Composites Science and Technology. 64:1261- 1278.

Berthelot, J.-M. (1999). Composite Materials. Mechanical Behavior and Structural Analysis. Springer, New York.

Chandra, R., Singh, S.P., Gupta, K. (1999). Damping Studies in Fiber-Reinforced Composites -A Review. Composite Structures 46: 41-51

El Mahi, A., Assarar, M., Sefrani, Y., Berthelot, J.-M. (2008). Damping Analysis of Orthotropic Composite Materials and Laminates, Composites B. 39(7) 1069-1076.

He S, Rao MD. (1992). Prediction of Loss Factors of Curved Sandwich Beams. Journal of Sound and Vibration. 159:101-113.

Meunier, M. and Shenoi, R.A. (2001). Dynamic Analysis of Composite Plates with Damping Modelled Using High-Order Shear Deformation Theory, Composite Structures, 54: 243–254.

Moser, K, Lumassegger, M. (1988). Increasing the Damping of Flexural Vibrations of Laminate FPC Structures by Incorporation of Soft Intermediate Plies with Minimum Reduction of Stiffness. Composite Structures. 10:321-333.

Nakra, BC (1984). Vibration Control with Viscoelastic Materials, III. The Shock and Vibration Digest.16:17-22.

Nakra, BC (1981). Vibration Control with Viscoelastic Materials, II. The Shock and Vibration Digest. 13:17-20.

Rikards, R. (1993) Finite Element Analysis of Vibration and Damping of Laminated Composites. Composite Structures. 24:193-204.

Vaswani, J, Asnani, NT, Nakra, BC (1988). Vibration and Damping Analysis of curved Sandwich Beams with a Viscoelastic Core. Composite Structures. 10:231- 245.

Mustapha Assarar is an Associate Professor at the University of Reims Champagne-Ardenne, France. He is a member of the Laboratory of Engineering and Materials Sciences (LISM). He obtained the PhD degree in Mechanical Engineering in the University of Maine in 2007. His research activities are developed in the fields of the mechanical behaviour, the damage and the vibrations of composite materials and structures. He also participates in the supervision of PhD students. His teaching activities concern the following domains: Mechanics of Rigid Bodies, Strength of Materials, Composite Materials, Finite Element and Mathematical.

Abderrahim El Mahi (born in 1962) is Professor at the Acoustics Laboratory of the University du Maine (LAUM). UMR CNRS 6613, France. After the completion of PhD in mechanics of composite materials in university de Poitiers (1991) (LMPM ENSMA), he obtained the habilitation to direct researches at the University du Maine (2002). Pr. A. EL MAHI's research includes mechanical behavior and damage of composite materials, solid mechanics, acoustic emission (AE), linear and non-linear vibration, finite element analysis. Pr. A. EL MAHI has supervised many PhD students in the framework of joint supervision with foreign universities. He regularly participates in PhD juries in France and abroad. Pr. A. EL MAHI teaches: Solid Mechanics, Composite Materials, Finite Element Analysis, Mechanical Design, Strength of Materials… at University du Maine, Le Mans, France.

Jean-Marie Berthelot is an Emeritus Professor at the Institute for Advanced Materials and Mechanics (ISMANS), Le Mans, France. His current research is developed in the fields of the Mechanical Behaviour of Composite Materials and Structures. He has published extensively works in the area of Composite Materials and is the author of an English textbook entitled "COMPOSITE MATERIALS. Mechanical Behavior and Structural Analysis" published by Springer, New York, in 1999, and two French textbooks: "MATÉRIAUX COMPOSITES. Comportement mécanique et analyse des structures, Tec & Doc Éditions, Paris, 5th edition (2012) and "MÉCANIQUE DES SOLIDES" Tec & Doc Éditions, Paris, 2nd edition (2006).

Textbooks on Composites and Mechanics are available from www.composites-mechanics.com.

Effect of Gold Nanoparticles Structural Variations on Mercury Removal

Khairul S.N. Kamarudin[*1], Mawarni F. Mohamad[2], Norfadilah Dolmat[3]

Faculty of Petroleum and Renewable Energy Engineering, Universiti Teknologi Malaysia

81310 UTM Johor Bahru, Malaysia

[*1]sozana@petroleum.utm.my; [2]mawarnifazliana@gmail.com; [3]nor.deela@gmail.com

Abstract

In this study gold nanoparticles with different size and shaped were synthesized by different methods in order to observe its capability to remove or adsorb mercury from the prepared solution. The results have showed that various sizes and shapes of gold nanoparticles were obtained using direct synthesis microwave polyol method and seed-mediated growth method. Small sized gold nanoparticles with spherical shapes were obtained by adding NaCl to the gold solution, whereas the seed-mediated growth method produced different shapes of gold nanoparticles with larger particle size. Using the same amount of mercury (20 ppm), the highest mercury removal (13,159 mg/g of gold) was acquired using spherical nanoparticles with particle size less than 10 nm.

Keywords

Gold Nanoparticles; Size and Shape; Mercury; Removal

Introduction

Mercury, a natural occurring element, could be present in various concentrations in natural gas. In natural gas condensate, mercury presents in a variety of forms (elemental, organometallic and inorganic salt), depending on the origin of the condensates. Although the concentrations of mercury in a given natural gas may be considered very low, but the cause is cumulative as it amalgamates. In the gas processing plant, aggregation of mercury can cause severe attack and failure of cryogenic aluminum heat exchangers resulting in a mechanical failure and gas leakage (Wilhem and Bloom, 2000). To provide a safe level of mercury, several approaches have been developed for the removal of mercury content in natural gas processing plant. Activated carbon is one of the adsorbents that widely used in gas purification, solvent recovery, and waste water treatment. The basic requirements for successful mercury removal are the economics of the process and the capability to reduce mercury concentrations to the acceptable level. The medium must have high capacity for an active bonding to mercury so that they can retain the mercury in a form that can be disposed. In addition, mercury removal system must be effective at the operational condition of the natural gas streams (El-Ela et al., 2006).

In addition, a good mercury adsorbent can also be used in monitoring the mercury level. The basic requirement for a good mercury monitoring system is that the sensor should be cost effective and suitable for mobile usage. Schambach et al. (2002) have developed mini mercury sensors that allow quick mobile analysis. The thickness of the gold structures used was approximately 40 nm and a total size of 2 mm x 2 mm of four meander-shaped of gold structures on the sensor chip. As mercury passes over the film, mercury amalgamates with the gold and interaction between gold and mercury leads to a change in the thin film resistivity. The total resistance will change continuously with increasing mercury concentrations in gold. It is important to note that the gold layer must be very thin to achieve a reasonable sensitivity (Schambach et al., 2002). Mozzaloi et al. (2004) has also reported that a micro fabricated physical sensor has been used for elemental mercury (Hg^o) detection in the air, based on the technique of resistivity variation of a gold thin film. In this sensor, adsorption process occurs when gold thin film is exposed to air polluted by mercury. After the measurement, the regeneration takes place and makes this sensor reusable for the next measurements. The duration of the regeneration depend not only on the quantity of adsorbed mercury but also the thickness of the gold layer. Thus, in addition to gold thin film, nanosized gold particles may offer a better adsorption characteristiscs that has effective adsorption.

Generally, the preparation of gold nanoparticles involves the chemical reduction of gold salt in solution. However, high surface energy of gold nanoparticles makes them extremely reactive, and the particles

undergo aggregation in the absence of any surface protection. Therefore, to produce gold nanoparticles, it is very important to avoid the aggregation of the particles. Several studies shows that gold nanoparticles have recently been synthesized under MW heating (400-1100 W) (Tu and Liu, 2000; Jiang et al., 2001; Pastoriza-Santos and Liz-Marzan, 2000; Liu et al., 2003). When $HAuCl_4.3H_2O$ or $HAuCl_4$ was reduced in methanol (Tu and Liu, 2000), ethanol (Jiang et al., 2001), N,N-dimethylformamide (Pastoriza-Santos and Liz-Marzan, 2000), water or sodium citrate (Liu et al., 2003), spherical nanoparticles with diameter below 85 nm were obtained. Tsuji et al. (2004) prepared a mixture of triangular, square, hexagonal, and close to the spherical gold nanoparticles by reduction of $HAuCl_4.4H_2O$ in ethylene glycol in the presence PVP under MW heating in continuous wave (CW) or pulse mode.

This paper presents various shapes and sizes of gold nanoparticles produced using direct synthesis microwave polyol method and seed-mediated growth methods. The percentage of mercury removal using gold nanoparticle has been measured. The amount of mercury removed indicates the performance of gold nanoparticles amalgamated with mercury.

Experimental

Microwave polyol method used was similar to that reported by Tsuji et al. (2004). Hydrogen tetrachloroaurate (III) hydrate ($HAuCl4.3H_2O$) was used as a source of gold particles, polyvinylprrolidone (PVP) as a protecting or capping agent, and ethylene glycol (EG) as both solvent and reductant. To obtain different sizes and shapes, gold nanoparticles was prepared by 4 different method; (1) by varying PVP concentration, (2) by adding NaCl to the gold solution, and (3) by seed-mediated growth method in which $HAuCl_4.3H_2O$ (denoted as $[Au]^1$) was added to gold seed (denoted as $[Au]^0$) at different ratio. The solution was then heated by microwave irradiation method to the boiling point of EG (198ºC) for 3 minutes. Another method (4) is by seed-mediated method using cetyl trimethylammonium bromide, (CTAB), sodium borohydride ($NaBH_4$), silver nitrate ($AgNO_3$) and ascorbic acid. The temperature of the growth medium was kept constant at 27-30°C.

Product particles were characterized by using transmission electron microscopy (JEOL JEM-2010 TEM). Before TEM analysis, PVP was separated from Au nanoparticles by centrifugation. In this case, the solution was diluted with ethanol and centrifuged at 10,000 rpm. Based on TEM photograph, the shape and size distribution of Au nanoparticles were calculated.

For the mercury adsorption, the precipitate (0.001 g) was added in 10 ml mercury solution. The percentage of mercury removed were determined by analyzing the concentration of mercury solution before and after the contacts with Au nanoparticles. The absorbance measurements were carried out by the atomic absorption spectrophotometer. (AAS, AAnalyst 400).

Result and Discussion

Gold Nanoparticles

Au nanoparticles were synthesized, characterized and evaluated for mercury adsorption performance. In the synthesis procedures, Au^{3+} salt is reduced to Au^0 to form activated species, either in a single step or via a Au+ intermediate followed by reduction to Au^0. These activated Au^0 species are thermodynamically unstable and rapidly aggregate to form nuclei and eventually formed the desired Au nanoparticle, as presented in Fig. 1. Au^{3+} salt is reduced to Au^0 to form activated species, either in a single step or via a Au^+ intermediate followed by reduction to Au^0. The definitions of shapes and sizes of gold nanoparticles are shown in Fig. 2.
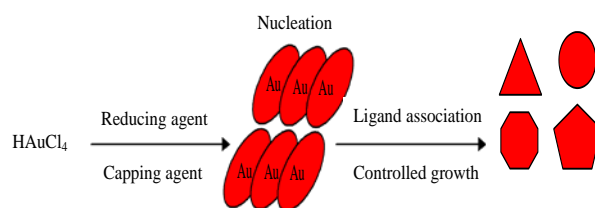

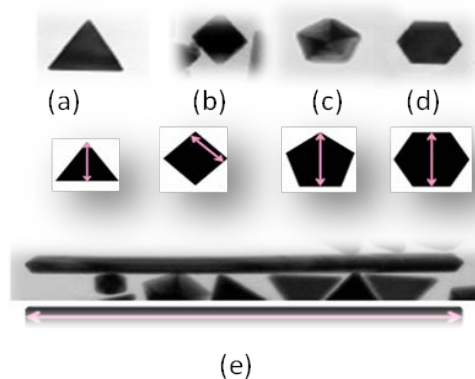FIG. 1 SCHEMATIC DIAGRAM OF AU NANOPARTICLES GROWTH (Lamer and Dinegar, 1950)

FIG. 2 DEFINITION OF SIZE OF GOLD NANOPARTICLE (a) TRIANGULAR (b) CUBIC (c) DECAHEDRAL (d) HEXAGONAL (e) 1 D PRODUCT (NANOROD) (Tsuji et al., 2004)

1) Effect of PVP Concentration

Gold nanoparticles were successfully prepared by varying PVP concentration and rapidly heated to 198°C. The particles were then characterized using transmission electron microscopy (TEM) to observe the sizes and the shape of the particles. The effect of PVP on the shape and size of gold nanoparticles is shown in Fig. 3, in which the size of gold nanoparticles decreases as PVP concentration increases. Using PVP 1.9 mM, the average particle size was 44 nm and then reduced to 6 nm when 22.2 mM of PVP was used. Similar average particle size was obtained using 33.3 mm of PVP. These particles have obtained sufficient protection by the capping agent (PVP) to prevent aggregation. The results also shows that a mixture of spherical, triangular, hexagonal, octahedral, decahedral, and icosahedral shapes were obtained using PVP concentration of 1.9 mM. The quantity of spherical shapes rises as the PVP concentration increases. By means of PVP concentration of 22.2 mM and above, the spherical shapes dominates (> 90%).
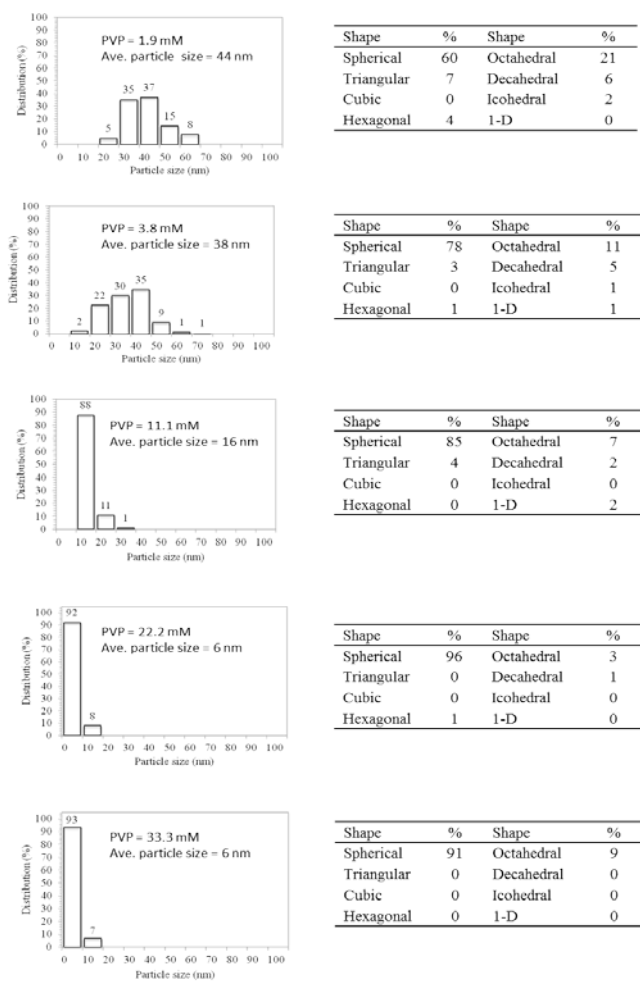
2) Effect of NaCl

The effects of NaCl on size and shape of Au nanoparticles are shown in Fig. 4. Significant changes have been observed in terms of the shape and the size of gold nanoparticles. A uniform distribution of Au nanoparticles was observed with the addition of 10 mM of NaCl, in which the size was mainly 10 nm or less. The addition of 20 mM of NaCl further increased the percentage of spherical nanoparticles to 99 % with the particle size less than 10 nm. According to Tsuji et al. (2007), oxidative etching occurred with the presence of both $AuCl_4^-$ and Cl^- ions to the surface of Au nanoparticles with more defect. Both ions have more opportunities to attack and further dissolve the unstable spherical nanoparticles. Fig. 5 illustrates Au nanoparticles obtained via addition of chloride ion.
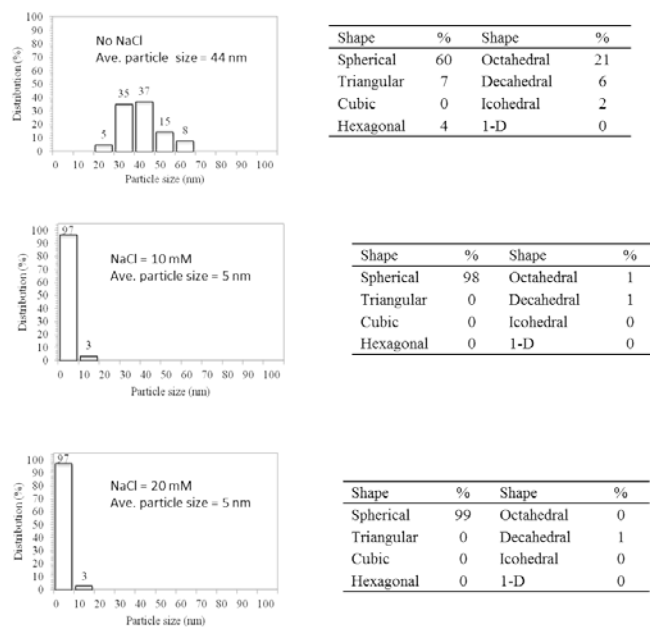

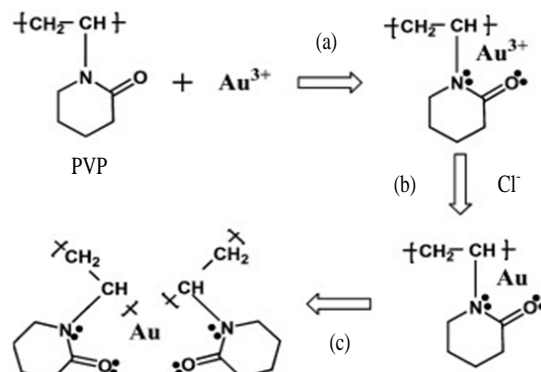FIG. 4 THE EFFECT OF CHLORIDE ION ON THE SHAPE AND SIZE OF GOLD NANOPARTICLE

FIG. 3 THE SIZE AND SHAPES OF AU NANOPARTICLES USING DIFFERENT PVP CONCENTRATIONS

FIG. 5 THE FORMATION OF STABLE GOLD NANOPARTICLES IN THE PRESENCE OF CHLORIDE ION

3)   Effect of $[Au]^1/[Au]^0$ Molar Ratio

The effects of $[Au]^1/[Au]^0$ on the sizes and shapes of Au nanoparticles are shown in Fig. 6. The size of Au nanoparticles rises as the $[Au]^1/[Au]^0$ molar ratio increases. There are also some changes in the shapes of gold nanoparticles formed. Initially, the Au seed mainly consist of spherical nanoparticles (85 %). The amount of spherical nanoparticles decrease but the size increases with increment of $[Au]^1/[Au]^0$ molar ratio. The changes on size and shape of Au nanoparticles are due to the etching and growth of Au nanoparticle from Au seed. The significant changes in size and shape of Au nanoparticles were observed by changing the $[Au]^1/[Au]^0$ molar ratio between 3 to 9.
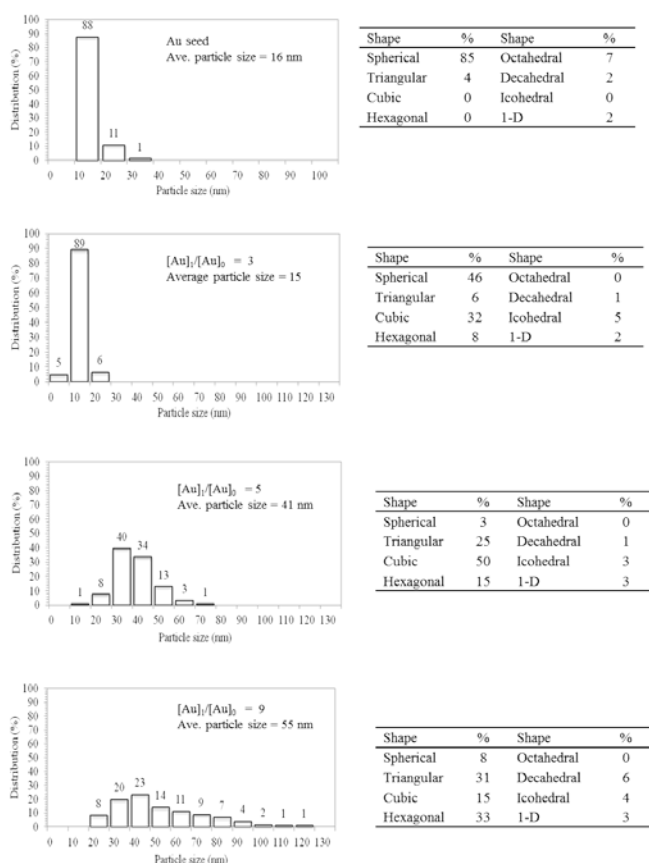

Shape	%	Shape	%
Spherical	85	Octahedral	7
Triangular	4	Decahedral	2
Cubic	0	Icohedral	0
Hexagonal	0	1-D	2

Shape	%	Shape	%
Spherical	46	Octahedral	0
Triangular	6	Decahedral	1
Cubic	32	Icohedral	5
Hexagonal	8	1-D	2

Shape	%	Shape	%
Spherical	3	Octahedral	0
Triangular	25	Decahedral	1
Cubic	50	Icohedral	3
Hexagonal	15	1-D	3

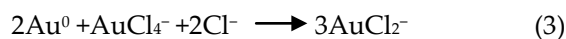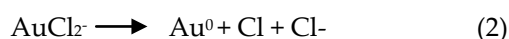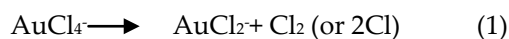| Shape	%	Shape	%
Spherical	8	Octahedral	0
Triangular	31	Decahedral	6
Cubic	15	Icohedral	4
Hexagonal	33	1-D	3

FIG. 6 THE EFFECT OF $[AU]^1/[AU]^0$ MOLAR RATIO TO THE SIZE AND SHAPE OF GOLD NANOPARTICLES

According to Tsuji et al. (2007), the reduction of $AuCl_4^-$ ions starts at 70°C (Eqn. 1) and further reduction occurs above ≈ 160°C (Eqn. 2). Therefore, two reaction sequence of reduction occurred in $AuCl_4^-$ ions. As reported by Rodr´ıguez-Fern´andez et al. (2005), the reaction of Au^0 metals were etched by $AuCl_4^-$ and Cl^- ions (Eqn. 3).

$$AuCl_4^- \longrightarrow AuCl_2 + Cl_2 \text{ (or 2Cl)} \qquad (1)$$

$$AuCl_2^- \longrightarrow Au^0 + Cl + Cl^- \qquad (2)$$

$$2Au^0 + AuCl_4^- + 2Cl^- \longrightarrow 3AuCl_2^- \qquad (3)$$

The completed decomposition of HAuCl4 is via two sequence reactions (Eqn. 1) and (Eqn. 2).

$$AuCl_4^- \longrightarrow Au^0 + Cl_2 + Cl + Cl^- \qquad (4)$$
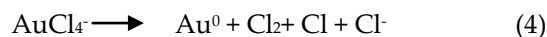
It was found that the decomposition of HAuCl4 in the present of Au^0 and Cl^- ion from first step reaction takes place in the second step reaction of $[Au]^1$ solution.

$$AuCl_4^- + 2Au^0 + 2Cl^- \longrightarrow 3AuCl_2^- \qquad (5)$$
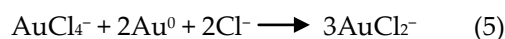
Reaction (5) was similar to Eqn. 3, reaction suggested by Rodr´ıguez-Fern´andez et al. (2005). The presence of both $AuCl_4^-$ and Cl^- ions in Au seeds solution resulted from oxidative etching of Au nanoparticles. In this study, the oxidative etching of spherical and octahedral nanoparticles was considered faster than other particles. As shown in Fig. 6, the formation of octahedral nanoparticles in Au seed is significantly less as compared to that of the spherical nanoparticles. The etching reaction was considered faster for octahedral particles and completely etched in the $[Au]^1/[Au]^0$ molar ratio of 3. Further etching reaction of spherical nanoparticles took place after octahedral nanoparticles completely etched producing other shapes.

Fig. 5 also shows that the size of gold nanoparticles becomes larger as the $[Au]^1/[Au]^0$ molar ratio increases. These results show that not only oxidative etching took place but the growth of Au nanoparticles was also involved. The oxidative etching occurred to spherical nanoparticles and at the same time, as the PVP concentration was not sufficient to coat and protect the the Au nanoparticles, the particles started to form larger gold nanoparticles. The growth rates of triangular and hexagonal plates, decahedral and icosahedral nanoparticles are faster than their etching rates, so they can survive and grow to larger nanoparticles.

Mercury Removal

The amount of mercury removed by using different size and shape of gold nanoparticles is shown in Table 1. Several samples have been selected to represent different shapes and size of gold nanoparticles. For particle size lower than 10 nm with 91% spherical shapes (sample 1A), the mercury removal is 5885 mg/g. However, for sample 1B, the amount of mercury adsorbed was significantly increased to 13159 mg/g. It is important to note that sample 1A consists of 91%

spherical and sample 1B has 99% spherical shape with particle size less than 10 nm. To further assess the performance of spherical nanoparticles, a comparison was made using particles size of 11-20 nm (Samples 1C and 1D). The result shows that using sample 1C with 85% spherical nanoparticles, the removal of mercury is 4977 mg/g but it decreased to 1541 mg/g as the percentage of spherical nanoparticles reduced to 46%. The results indicated that sample with high yield of spherical nanoparticles has the ability to absorb more mercury than that with other polygonal shapes.

TABLE 1 MERCURY REMOVAL USING DIFFERENT SIZE AND SHAPE OF GOLD NANOPARTICLES

Sample No.	Shape	Quantity (%)	Amount (mg/g)
Gold nanoparticles ≤ 10 nm			
1A	Spherical	91	5885
	Triangular, hexagonal	0	
	Octahedral, decahedral, icosahedral	9	
1B	Spherical	99	13,159
	Octahedral, decahedral, icosahedral	1	
Gold nanoparticle size range 11-20 nm			
1C	Spherical	85	4977
	Triangular, hexagonal	4	
	Octahedral,Decahedral, Icosahedral	7	
	1-D	2	
1D	Spherical	46	1541
	Triangular, hexagonal	14	
	Cubic	32	
	Octahedral,Decahedral, Icosahedral	6	
	1-D	2	
Gold nanoparticle size range ≥ 21 nm			
2A	Spherical	10	2837
	Triangular, hexagonal	57	
	Cubic	25	
	Octahedral,Decahedral, Icosahedral	5	
	1-D	3	
2B	Spherical	8	2205
	Triangular, hexagonal	64	
	Cubic	15	
	Octahedral,Decahedral, Icosahedral	10	
	1-D	3	
2C	1-D (Nanorod)	94	3331

The results of mercury removal with particle size greater than 21 nm are represented by samples 2A and 2B. The yield of spherical nanoparticles and 1-D products in samples 2A and 2B are almost of the same amount. However, the results have showed that the amount of mercury removed by sample 2A is slightly higher (2837 mg/g gold nanoparticles) than that in sample 2B (2205 mg/g gold nanoparticles), which might be due to variation of polygonal particles. The results also indicated that it is rather difficult to assess the performance of polygonal particles since the sample does not represent any dominant shape of polygonal particles. However, seed-mediated growth method that has produced nanorod (sample 2C) gives higher amount of mercury removal per gram gold nanoparticles as compared to the other two samples (samples 2A and 2B).

Conclusions

Microwave polyol method would be a suitable method resulting from its simple and rapid procedure of producing gold nanoparticles. The great advantage of microwave heating is that a short crystallization time is needed to produce Au nanoparticles. PVP plays a role as a capping agent to avoid aggregation. Further, the addition of NaCl to the gold solution has produced smaller nanoparticles (less than 10 nm). However, the polygonal shapes have been obtained by seed-mediated growth method. The study showed that the particle size played a significant role in mercury removal. With the size of gold nanoparticles less than 10 nm, the spherical gold nanoparticles removed the highest amount of mercury (13,159 mg/g). This is due to the fact that for the same amount of gold nanoparticles used, small size particles could provide high surface area for mercury to be adsorbed on its surfaces and that other polygonal shapes are larger but with lower adsorption capacity compared to spherical shapes. Therefore, smaller sized gold nanoparticles can be obtained using microwave polyol method by means of the addition of NaCl to the gold solution. These gold nanoparticles adsorb high amount of mercury in the prepared solution.

REFERENCES

El-Ela, A. Mahmoud, Mahgoub , Nabawi, Mostafa and Aziem, A. Mohamed "Eqytian Gas Plant Employs Adsorbents for Hg Removal." Oil and Gas Journal. 104 (2006): 52-58.

Jiang, Zhi-Liang, Feng Zhong-Wei and Shen Xing-Chan,

"Microwave Synthesis of Au Nanoparticles with the System of AuCl4-CH3CH2OH." Chinese Chemistry Letter 12 (2001): 551-554.

Lamer, Victor K. and Dinegar Robert H., "Theory, Production and Mechanism of Formation of Monodispersed Hydrosols." Journal of American Chemical Society. 72 (1950): 4847-4854.

Liu, Fu K., Ker Chu J., Chang Yu C., Ko Fu H., Chu Tieh C. and Dai Bau T., "Microwave Heating for the Preparation of Nanometer Gold Particles." Japanese Journal of Applied Physics 42 (2003): 4152-4158.

Mazzolai, Barbara, Mattoli Virgilio, Raffa Vittoria and Tripoli Girolamo, "A Microfabricated Physical Sensor for Atmospheric Mercury Monitoring." Sensors and Actuators, 113 (2004): 282-287.

Pastoriza-Santos, Isabek and Liz-Marzan M. Luis, "Formation of PVP-Protected Metal Nanoparticles in DMF." Langmuir 18 (2002): 2888-2894.

Rodríguez, J. Fernández, Pérez, J. Juste, Mulvaney, P. and. Liz-Marzán, L. M, "Spatially-Directed Oxidation of Gold Nanoparticles by Au(III)–CTAB Complexes." The Journal of Physical Chemistry. B, 109 (2005): 14257-14261.

Schambach, Kwan, Eden Klaus, Schumacher Klaus and Wigleb Gerhad, "Micromachined Mercury Sensor." in Proceeding of the 32nd European Solid-State Device Research Conference, Firenze, Italy, 2002.

Tsuji Masaharu, Hashimoto Masayuki, Nishizawa Yuki and Tsuji Takeshi. "Synthesis of Gold Nanorods and Nanowires by Microwave-polyol Method," Materials Letter, 58 (2004): 2326-2330.

Tsuji, Masaharu, K. Matsumoto, N. Miyamae, T. Tsuji and X. Zhang, "Rapid Preparation of Silver Nanorods and Nanowires by a Microwave-Polyol Method in the Presence of Pt Catalyst and Polyvinylpyrrolidone," Crystal Growth & Design. 7 (2007): 311-320.

Tu, Weixia and Liu Hantan, "Rapid Synthesis of Nanoscale Colloidal Metalclusters by Microwave Irradiation." Journal of Materials Chemistry 10 (2000): 2207-2211.

Wilhelm, S. Mark and Bloom Nicholas, "Mercury in Petroleum." Fuel Processing Technology, 63 (2000): 1-27.

Khairul S.N. Kamarudin graduated from University of New South Wales, Australia. In 1991, she joined Universiti Teknologi Malaysia as an Assistant Lecturer. She received her PhD degree in 2006 and curently being an associate professor at the Faculty of Petroleum and Renewable Energy, Universiti Teknologi Malaysia. Her research interests are in advanced material and separation processes.